



**HAL**  
open science

# Adaptive deformation of 3D unstructured meshes with curved body fitted boundaries with application to unsteady compressible flows

Luca Cirrottola, Mario Ricchiuto, Algiane Froehly, Barbara Re, Alberto Guardone, Giuseppe Quaranta

## ► To cite this version:

Luca Cirrottola, Mario Ricchiuto, Algiane Froehly, Barbara Re, Alberto Guardone, et al.. Adaptive deformation of 3D unstructured meshes with curved body fitted boundaries with application to unsteady compressible flows. *Journal of Computational Physics*, 2021, 433, pp.110177. 10.1016/j.jcp.2021.110177 . hal-03194100

**HAL Id: hal-03194100**

**<https://inria.hal.science/hal-03194100>**

Submitted on 9 Apr 2021

**HAL** is a multi-disciplinary open access archive for the deposit and dissemination of scientific research documents, whether they are published or not. The documents may come from teaching and research institutions in France or abroad, or from public or private research centers.

L'archive ouverte pluridisciplinaire **HAL**, est destinée au dépôt et à la diffusion de documents scientifiques de niveau recherche, publiés ou non, émanant des établissements d'enseignement et de recherche français ou étrangers, des laboratoires publics ou privés.

1 Adaptive deformation of 3D unstructured meshes  
 2 with curved body fitted boundaries with  
 3 application to unsteady compressible flows

4 Luca Cirrottola<sup>a</sup>, Mario Ricchiuto<sup>a</sup>, Algiane Froehly<sup>b</sup>, Barbara Re<sup>c</sup>, Alberto  
 5 Guardone<sup>d</sup>, Giuseppe Quaranta<sup>d</sup>

6 <sup>a</sup>*INRIA, Univ. Bordeaux, CNRS, Bordeaux INP, IMB, UMR 5251, 200 Avenue de la Vieille Tour,*  
 7 *33405 Talence cedex, France*

8 <sup>b</sup>*INRIA Direction Générale Déléguée à l'Innovation, France*

9 <sup>c</sup>*Institute of Mathematics, University of Zürich, 8057 Zürich, Switzerland*

10 <sup>d</sup>*Department of Aerospace Science and Technology, Politecnico di Milano, 20156 Milano, Italy*

---

11 **Abstract**

12 We present an adaptive moving mesh method for unstructured meshes which is a three-  
 13 dimensional extension of the previous works of Ceniceros et al. [10], Tang et al. [40]  
 14 and Chen et al. [11]. The iterative solution of a variable diffusion Laplacian model on  
 15 the reference domain is used to adapt the mesh to moving sharp solution fronts while  
 16 imposing slip conditions for the displacements on curved boundary surfaces. To this  
 17 aim, we present an approach to project the nodes on a given curved geometry, as well as  
 18 an a-posteriori limiter for the nodal displacements developed to guarantee the validity  
 19 of the adapted mesh also over non-convex curved boundaries with singularities.

We validate the method on analytical test cases, and we show its application to  
 two and three-dimensional unsteady compressible flows by coupling it to a second order  
 conservative Arbitrary Lagrangian-Eulerian flow solver.

20 *Keywords:* Constant-connectivity mesh adaptation, unstructured meshes, unsteady  
 21 compressible flows, conservative formulations.

---

22 **1. Introduction**

sec:Intro

23 Mesh adaptation is a powerful tool to improve the representation of complex fields for  
 24 a given computational expense. In computational fluid dynamics in particular, adapta-  
 25 tion has become nowadays a customary tool [37]. Adapting the mesh also has a relative  
 26 computational overhead, which motivates the quest for efficient and robust methods.

27 Techniques improving the discrete representation of the fields of interest by inserting  
 28 and removing mesh entities (so called h-adaptation) have proven to be quite mature [37].  
 29 However, solution transfer between meshes with different topologies may be non-trivial  
 30 and may have a non-negligible computational cost, especially if conservation constraints  
 31 need to be satisfied [19, 3, 25, 32, 38].

32 By contrast, mesh nodes relocation with constant element connectivity (so called  
 33 r-adaptation), offers the possibility of a minimally intrusive coupling with existing com-

34 putational mechanics solvers, as no modification of the data structures is required. As  
 35 h-adaptation methods, they also provide considerable improvement in the quality of  
 36 the solutions obtained, especially in unsteady simulations of traveling waves, like shock  
 37 waves and water waves, where uniform refinement would be way too costly. More-  
 38 over, with r-adaptation methods devising conservative projections is much simpler. In  
 39 fact, the preservation of the one-to-one mapping from the old to the new mesh entities  
 40 allows the easy construction of a conservative remapping [33], or the use of Arbitrary-  
 41 Lagrangian-Eulerian (ALE) formulations compliant with the Geometric Conservation  
 42 Law (GCL) [48, 43].

43 Unfortunately, the preservation of the initial mesh topology undeniably imposes se-  
 44 vere restrictions on nodal displacements in order to avoid mesh folding with tangled (i.e.  
 45 inverted) elements, especially when the boundary exhibits singular points. Moreover,  
 46 the accuracy attainable for complex solutions is limited by the initial density of mesh  
 47 nodes, and less finely-tunable than in metric-based h-adaptation [2].

48 Anyway, the advantages brought by the effortless coupling with external flow solvers  
 49 and the conservative solution remapping can counterbalance the mesh quality limitation  
 50 as long as the r-adaptation technique is computationally efficient. Simply put, the error  
 51 reduction brought by adapting the mesh must offset the computational overhead. A  
 52 measure of this efficiency can be evaluated by comparing with the cost of a simulation  
 53 run on a uniformly refined mesh, providing the same resolution of the flow field. Hybrid  
 54 adaptive approaches combining well timed re-meshing and adaptive deformation at every  
 55 time step, which are perhaps the ones computationally most appealing, still require the  
 56 r-adaptation step to perform well.

57 Extensive reviews of r-adaptation can be found in [31, 9]. We focus here on methods  
 58 based on the numerical solution of an elliptic partial differential equation for the posi-  
 59 tion of the mesh nodes, often referred to as the mesh PDE. This equation is typically  
 60 formulated to find a mapping  $\xi : \Omega_{\mathbf{x}} \rightarrow \Omega_{\xi}$  from the physical domain to a reference (com-  
 61 putational) one. This mapping needs to be injective and surjective in order to guarantee  
 62 that the produced mesh neither folds nor breaks the domain. Historically the Winslow  
 63 or homogeneous Thompson-Thames-Mastin generator [45, 46]  $\Delta_{\mathbf{x}}\xi = \mathbf{0}$  has been the  
 64 basis for structured boundary-fitted grid generation (see for example the review in [44])  
 65 and it has been extended to also adapt the mesh in the domain either by adding source  
 66 terms to the equation, or through a variable-diffusion approach [52]. A more general  
 67 formulation of the last method has been given in [15] by means of harmonic maps and  
 68 extended in [7].

69 These equations describe the mapping  $\xi = \xi(\mathbf{x})$  and need to be inverted for the  
 70 physical coordinates  $\mathbf{x} = \mathbf{x}(\xi)$ , leading to a nonlinear system of PDEs which is iteratively  
 71 solved. In order to ease the cost of the iterative solution of the inverted equations, an  
 72 alternative mesh generator was proposed in [10] based on a variable-diffusion Laplace  
 73 equations directly formulated in the physical domain for the mapping  $\mathbf{x} : \Omega_{\xi} \rightarrow \Omega_{\mathbf{x}}$ .  
 74 This generator is not based on a theoretical derivation, but on the observation that the  
 75 variable-diffusion Laplacian in the reference domain is sufficient to adapt the mesh in  
 76 the desired regions while the equations, which are still nonlinear, can easily be solved  
 77 through a relaxation procedure. The efficiency of the method was shown in application

78 to two-dimensional Boussinesq convection on structured grids, and the method was later  
79 applied in [40] to hyperbolic conservation laws and extended in [11] to multicomponent  
80 flows on two-dimensional unstructured grids. More recently, the same method was  
81 applied to the two-dimensional shallow water equations both in Cartesian and spherical  
82 coordinates [4, 5, 6].

83 Robustness to mesh folding in r-adaptation is a delicate matter, similarly critical in  
84 the context of mesh deformation related to moving boundaries, curved mesh generation  
85 and smoothing (see for example [30, 16, 47, 20, 49]). Obtaining non-singular meshes  
86 requires two main conditions to be met. The first is that the continuous map, appro-  
87 priately modified to account for all boundary conditions, should verify the appropriate  
88 conditions as e.g. the non-negativity of the determinant of the deformation Jacobian.  
89 Until quite recently, sufficient conditions were known only in the framework of harmonic  
90 maps [15, 35]. Recent work by [27], has allowed to prove similar properties for other  
91 types of mesh PDEs, as e.g. some of those proposed by Huang [26] or Huang and Rus-  
92 sel [28], by resorting to energy arguments borrowed from the theory of gradient flows.  
93 The second important aspect is that the discretization used to approximate the mesh  
94 PDE should have the appropriate “property preserving” character, so that the fully  
95 discrete moving mesh method is also guaranteed to provide non-singular meshes. This  
96 is in itself a subject of investigation. It is in general well known that discrete moving  
97 mesh methods can lead to mesh tangling even with properly chosen mesh PDEs [15],  
98 and the impact of the truncation error is stressed for example in [31]. In the setting of  
99 gradient flow maps, geometrical discretizations have been shown in [27] to answer the  
100 discrete positive Jacobian requirement. However, even in the last reference, the issue of  
101 accounting for complex curved boundaries is overlooked, even though mesh movement  
102 along a given surface does not appear to be necessarily a natural boundary condition of  
103 the PDEs considered.

104  
105 In this work we proceed differently. We want to be able to handle domains with  
106 boundaries as general as possible in three space dimensions. and propose a relaxation  
107 technique embedding a geometrical limiter allowing to achieve this objective. We focus  
108 on the simple reference-domain variable-diffusion Laplacian approach originally pro-  
109 posed in [10], however the ideas proposed in this paper can be extended to other mesh  
110 PDEs. To the best of the authors’ knowledge, very few applications of r-adaptation to  
111 three-dimensional meshes are available to date, see for example [34] as well as some  
112 simple applications in [27]. The original approach in [10] does not offer theoretical guar-  
113 antees against folding, although it has been successfully used in many applications with  
114 non-convex boundaries. R-adaptation in three dimensions exhibits even stronger limi-  
115 tations than in two dimensions, as sufficiency results for unfolded continuum maps are  
116 typically based on requirement of smoothness and convexity of the boundary. These are  
117 easily violated especially in application to external flows, where the boundary is not con-  
118 vex and several singularities (like corners and ridges) are present. We have experienced  
119 that tangling is a major concern in the three-dimensional extension of these techniques.  
120 Smoothing or untangling methods for unstructured meshes already developed in the  
121 literature require nontrivial procedures [24, 47].

122 Our contribution is thus related to a mesh displacement method allowing to guar-  
 123 antee that nodes move and always remain on a given parametrizaion of curved domain  
 124 boundaries, and for an *a-posteriori* limiter for the nodal displacement which, when em-  
 125 bedded in the mesh relaxation iterations, allows to prevent the occurrence of tangled  
 126 elements, thus enforcing the validity of the discrete mapping while avoiding smoothing  
 127 procedures. The resulting moving mesh library `Fmg` has been developed on top of the  
 128 open source software `Mmg` <sup>Papogny2014, MmgSW</sup> [12, 1] to exploit, among other things, its built-in cubic Bézier  
 129 patch representation of complex manifolds.

130 The paper is organized as follows. We recall the continuous mesh partial differential  
 131 equations in section §2, while a thorough discussion of their numerical solution is given  
 132 in section §3, including a-posteriori limiting and projections to obtain a valid mesh  
 133 satisfying all the boundary conditions, and the application to unsteady simulations.  
 134 We discuss the validation of the method proposed considering the adaptation w.r.t.  
 135 analytical functions in two and three space dimensions in section §4, and application  
 136 to two and three dimensional unsteady compressible flows are discussed in section §5  
 137 Finally, conclusions are presented in section <sup>sec:Conclusions</sup> 6.

## 138 2. Variable-diffusion Laplacian r-adaptation in the reference domain

sec:NumModel

139 We focus here on Laplacian-based r-adaptation, which is the mesh PDE currently  
 140 implemented in the `Fmg` library. However, the ideas proposed in this paper can be  
 141 immediately extended to other mesh PDEs. We recall here the continuous mesh problem,  
 142 and in particular we discuss the boundary conditions, as well as the definition of the  
 143 monitor functions used for adaptation.

144 Following <sup>Chen2008</sup> [11], we look for a mapping  $\mathbf{x} : \Omega_\xi \rightarrow \Omega_{\mathbf{x}}$  from the reference domain  $\Omega_\xi$   
 145 (the original mesh) to the computational domain  $\Omega_{\mathbf{x}}$  (the adapted mesh). Within the  
 146 reference domain, the computational coordinates satisfy the variable-diffusion Laplace  
 147 equation

$$\nabla_\xi \cdot (\omega(\mathbf{x}) \nabla_\xi \mathbf{x}) = 0 \quad \text{in } \Omega_\xi \quad \text{eq:rLap} \quad (1)$$

148 The above problem is in general a system of coupled non-linear PDEs, which needs to be  
 149 complemented by appropriate boundary conditions. Nonlinearity is introduced by the  
 150 monitor function  $\omega(\mathbf{x})$  which depends on an external field evaluated in the computational  
 151 domain. In this work, we have used a classical scalar definition for this quantity, which  
 152 allows to decouple the equations for the three spatial coordinates.

153 In particular, given a quantity of interest  $f(\mathbf{x})$ , the scalar monitor function used in  
 154 the examples discussed later is evaluated as

$$\omega(\mathbf{x}) = \sqrt{1 + \alpha \|\nabla_\xi f(\mathbf{x})\|_{\gamma_\alpha}^2 + \beta \|\mathbf{H}_\xi(f)(\mathbf{x})\|_{\gamma_\beta}^2 + \tau \|f\|_{\gamma_\tau}^2} \quad \text{eq:monitorFunction} \quad (2)$$

155 where  $\nabla_\xi$  and  $\mathbf{H}_\xi$  denote the gradient and Hessian computed on the reference domain  
 156  $\Omega_\xi$ . Norm  $\|f\|_\gamma$  is defined as

$$\|f\|_\gamma = \min \left( 1, \frac{\|f\|}{\gamma \max(\|f\|)} \right). \quad (3)$$

157 This normalization, already used in [Chen2008](#)  
158 norm maximum according to the value of  $\gamma$ . The idea behind this normalization is to  
159 spread a little bit the peak values of the function  $f$  around the peak locations, in order  
160 to filter out small inhomogeneities in the numerical approximation of the sharp fronts of  
161  $f$ . The above definition gives the user some control on the behaviour of the spatial map-  
162 ping via the parameter pairs  $(\alpha, \gamma_\alpha)$ ,  $(\beta, \gamma_\beta)$ ,  $(\tau, \gamma_\tau)$ . As in the original works [Genieiros2001, Chen2008](#),  
163 these parameter pairs are not related to an error estimate, thus they are determined  
164 empirically and they are intrinsically dependent on the application. However, in our  
165 experience a short test on a few time steps is sufficient to assess the behaviour of these  
166 parameters on the whole simulation time range.

### 2.1. Boundary conditions

sec:NumModelBCs  
169 Despite the decoupling of equation [\(1\)](#) into separate scalar equations, even for a  
170 scalar monitor function a strong coupling of the coordinate equations may arise through  
171 the boundary conditions, especially in domains including general shapes. In particular,  
172 we will split the boundary on two parts as  $\partial\Omega_\xi = \Gamma_\xi^D \cup \Gamma_\xi^S$ . A full set of Dirichlet  
173 conditions are imposed on  $\Gamma_\xi^D$

$$\mathbf{x} = \boldsymbol{\xi} \quad \text{on } \Gamma_\xi^D \quad (4)$$

174 as this is the portion of the boundary that is not allowed to move. Since fixed boundary  
175 nodes are not convenient whenever adaptation is performed on flow waves approach-  
176 ing the boundary, we want to limit as much as possible usage of Dirichlet conditions,  
177 preferring slip boundary conditions wherever we can formulate them while preserving  
178 sharp geometrical features of the boundary. Along the *slip* boundary  $\Gamma_\xi^S$  the coordinate  
179 positions are constrained to move along a given parameterized domain. For manifold sur-  
180 faces, we assume to have a known parameterization, for example in the form  $\gamma^S(\mathbf{x}) = 0$ .  
181 This provides one **position** constraint relating the  $d$  spatial coordinates. Thus,  $d-1$  addi-  
182 tional conditions are required, which are here taken as the null normal stress conditions  
183 parallel to the local tangent space spanned by  $\{\hat{\boldsymbol{\tau}}_j^S\}_{j=1, d-1}$ . This gives the boundary  
184 conditions:

$$\begin{aligned} \gamma^S(\mathbf{x}) &= 0 \\ \hat{\mathbf{n}}^S \cdot (\omega(\mathbf{x}) \boldsymbol{\nabla} \mathbf{x}) \cdot \hat{\boldsymbol{\tau}}_j^S &= 0 \quad \forall j = 1, d-1 \end{aligned} \quad \text{on } \Gamma_\xi^S \quad (5) \quad \text{eq:manifold-bc}$$

185 In three dimensions, the slip boundary  $\Gamma_\xi^S$  can be further generalized as the union  
186 of multiple manifolds with one-dimensional boundaries joining them. This leads to  
187 intersection curves where two sets of equations [5](#) should formally be satisfied at the  
188 same time, constraining the displacement to happen along the curve tangent direction.  
189 Points where multiple intersection curves meet are corner points and no displacement  
190 is possible, thus Dirichlet conditions are imposed on (and only on) these points. The  
191 approach used here for the numerical enforcement of boundary conditions is discussed  
192 in the following section.

193

### 3. Discrete equations, a-posteriori limiting, slip on curved boundaries

sec:NumModel1

194

195

196

197

198

199

200

We discuss here the implementation choices made in the `Fmg` library, namely the discretization of the mesh PDEs, as well as their iterative solution. Both the a-posteriori limiting of the displacement and the implementation of the slip boundary conditions are strongly tied to the relaxation iterations, and for this reason all the steps are discussed in this section. More specifically, to relieve the complexity of satisfying the boundary conditions (5), we formulate the discrete approximation by means of an iterative multiple-corrections procedure embedding the following three elements:

201

202

203

204

205

1. A finite element approximation of the variational form of (II) with natural (Neumann) boundary conditions;
2. An a-posteriori limiter for the nodal displacement enforcing local mesh validity;
3. A boundary correction in the local normal direction to enforce the first of (5) by projecting on the manifold parametrization **at hand**.

206

207

208

209

210

211

212

213

214

215

216

The intertwining of the a-posteriori limiter of the displacement, of the update of the local boundary normals, and of the projection on the parameterized manifold is essential for the proposed approach to provide valid adapted meshes both in the volume and on the boundaries.

Concerning the representation of these, the `Fmg` library we developed makes use of the point-normal curved triangles parameterization proposed in [51], which is based on cubic Bézier patches with quadratically varying normals. For this we leverage the implementation provided by the open source software `Mmg` [12, 1]. However note that the form of the manifold parametrization is not a necessary ingredient of our method. Other high order approximations can be used.

217

#### 3.1. Finite element approximation: Dirichlet and natural boundary conditions

sec:weak

218

219

220

The discrete equations are built starting from a linear finite element approximation of the problem embedding **natural (Neumann) boundary conditions**, which corresponds to the simple variational form

$$\int_{\Omega_\xi} \omega(\mathbf{x}) \nabla_\xi v \cdot \nabla_\xi \mathbf{x} \, d\Omega_\xi = \mathbf{0}, \quad \forall v \in H^1(\Omega_\xi). \quad (6) \quad \text{eq:var-rlap}$$

221

222

223

224

225

226

227

228

Note that this statement satisfies the **null normal stress conditions** in (5) but neither the remaining one in the system (the belonging to the surface), nor any Dirichlet conditions eventually assigned. Dirichlet conditions are strongly imposed on the solution space, while the enforcement of the belonging to a slip surface will be detailed in the following 3.4) Note also that  $\omega$  being a scalar quantity, the above equations provide uncoupled nonlinear variational statements for each component of  $\mathbf{x}$ .

The projection of (6) on the linear finite element space leads to the nonlinear algebraic system

$$\mathbf{K}(\mathbf{x}) \mathbf{x}^\nu = \mathbf{0}, \quad \nu = 1, \dots, d \quad (7) \quad \text{eq:fem1}$$

229 having introduced the array of unknown node positions  $\mathbf{x}^\nu = [x_i^\nu]$  for each space com-  
 230 ponent  $\nu$ , with  $d$  the number of space dimensions, and where the stiffness matrix has  
 231 the standard entries

$$K_{ij}(\mathbf{x}) = \int_{\Omega_\xi} \omega(\mathbf{x}) \nabla_\xi \phi_i \cdot \nabla_\xi \phi_j \, d\Omega_\xi \quad (8) \quad \text{eq:stiffLap}$$

232 with  $\{\phi_i\}_{i \geq 1}$  the linear base functions spanning the solution space. Please note that (7)  
 233 is a set of decoupled systems, one for each spatial direction, as shown by the fact that  
 234  $K_{ij}$  are scalar entries. Note also due to the consistency of the finite element space with  
 235 Dirichlet conditions, Dirichlet nodes are not included in the above sum.

236 In practice, by defining the displacement  $\boldsymbol{\delta} = \mathbf{x} - \boldsymbol{\xi}$ , the system is not written as in  
 237 (7), but as

$$\mathbf{K}(\mathbf{x}) \boldsymbol{\delta}^\nu = -\mathbf{K}(\mathbf{x}) \boldsymbol{\xi}^\nu \quad (9) \quad \text{eq:fem2}$$

238 which is better suited for the iterative corrections described in the following sections.

### sec:Jacob39 3.2. Scalar correction iterations

240 We introduce an iterative procedure which, while avoiding mesh tangling in 2D  
 241 and 3D, and accounting for the directional coupling inherent to (5), retains the scalar  
 242 structure of the decoupled variational form. Note however that the corrections proposed  
 243 can be easily adapted to other iterative solution methods (as well as mesh PDEs).

244 The basic iteration used in our method starts from a standard diagonal Jacobi re-  
 245 laxation to handle the nonlinearity of (9)

$$K_{ii}^{[k]} \boldsymbol{\delta}_i^{[k+1]} = - \sum_{\substack{j \in \mathcal{B}_i \\ j \neq i}} K_{ij}^{[k]} \boldsymbol{\delta}_j^{[k]} - \sum_{j \in \mathcal{B}_i} K_{ij}^{[k]} \boldsymbol{\xi}_j \quad (10)$$

246 where  $\mathcal{B}_i$  denotes the ball<sup>1</sup> of node  $i$  and vector  $\boldsymbol{\delta}_i^{[k]} = [\delta_i^\nu]_{\nu=1, \dots, d}$  is now the vector made  
 247 of the space components of the displacement of node  $i$  at iteration  $k$  (the same notation  
 248 will be used for vectors  $\mathbf{x}_i$  and  $\boldsymbol{\xi}_i$ ). Again, we stress that the above iteration is in fact  
 249 a set of  $d$  relations for the components of the displacement. The matrix entries  $K_{ij}^{[k]}$   
 250 depend on monitor function  $\omega$  at iteration  $k$  (cf. equation (8)), which in turn depends  
 251 on the scalar field  $f$  evaluated at the actual positions  $\mathbf{x}_i^{[k]}$ , according to equation (2). In  
 252 our current implementation, the re-evaluation is performed by linearly interpolating the  
 253 scalar field  $f$  at the current nodal positions  $\mathbf{x}_i^{[k]}$  through a standard search algorithm  
 254 based on barycentric coordinates.

255 In our implementation we added and removed the term  $K_{ii}^{[k]} \boldsymbol{\delta}_i^{[k]}$ , to obtain the fol-  
 256 lowing iterations

$$\boldsymbol{\delta}_i^{[k+1]} = \boldsymbol{\delta}_i^{[k]} - \frac{1}{K_{ii}^{[k]}} \sum_{j \in \mathcal{B}_i} K_{ij}^{[k]} \mathbf{x}_j^{[k]} \quad (11)$$

<sup>1</sup> In the common lexicon of the mesh generation community, the ball  $\mathcal{B}_i$  of a mesh node  $i$  is defined here as the set of elements sharing vertex  $i$  [21]. To ease the notation, with a slight abuse of terminology we say that a node  $j$  belongs to the ball of node  $i$  if it is a vertex of an element belonging to the ball, and we denote this statement as  $j \in \mathcal{B}_i$ .



257 which are initialized with  $\delta_i^{[0]} = \mathbf{0}$ .

258 The last step is the computation of the new nodal positions as follows

$$\mathbf{x}_i^{[k+1]} = \mathbf{x}_i^{[k]} + \widetilde{\Delta \mathbf{x}}_i^{[k+1]} \left( \delta_i^{[k+1]}, \{\mathbf{x}_i^{[k+1]}\}_{j < i}, \{\mathbf{x}_i^{[k]}\}_{j \geq i} \right) \quad (12)$$

259 where  $\widetilde{\Delta \mathbf{x}}_i^{[k+1]}$  are limited increments obtained by a-posteriori correcting  $\delta_i^{[k+1]}$  to ac-  
 260 count for both mesh validity and boundary conditions (both Dirichlet and slip wall).  
 261 In both cases, these corrections are local, albeit not only dependent on node  $i$ , and  
 262 non-linear w.r.t.  $\mathbf{x}$ . The nonlinearity is readily handled in the iterations by using the  
 263 last nodal positions available.

`sec:relax`

### 3.3. A-posteriori corrections for mesh validity enforcement

265 The Laplacian model in the reference domain does not guarantee that the Jacobian  
 266 of the mapping is strictly positive everywhere, thus leading to the occurrence of tangled  
 267 (invalid) mesh elements. In two space dimensions, our experience has shown that in  
 268 most cases carefully tuning the monitor function  $\omega(\mathbf{x})$  allows to solve this issue. This is  
 269 not the case in three dimensions, where tangling occurs much more often.

270 To cope with this, we have devised an a-posteriori limiter to the nodal displacements  
 271 which is activated whenever the displacement of a node causes the occurrence of an  
 272 element whose volume is below a given threshold. This condition is of course implicit,  
 273 in the sense that it couples the positions of all the mesh nodes. However, it can be  
 274 easily embedded in an iterative setting. In particular, in our implementation we relax  
 275 and update each nodal position  $\mathbf{x}_i^{[k+1]}$ , one after the other. As illustrated on figure `fig:relax`  
 276 (for simplicity in 2D), each displacement  $\delta_i^{[k+1]}$  is limited according to the validity of  
 277 the configuration in the current ball  $\mathcal{B}_i^{[k,k+1]}$  obtained using new values  $\{\mathbf{x}^{[k+1]}\}_{j < i}$ , for  
 278 nodes updated before  $i$ , and old positions  $\{\mathbf{x}_j^{[k]}\}_{j > i}$  for nodes not updated yet. This  
 279 relax-update step has a *Gauss-Seidel* flavour, as the position of each node is updated  
 280 based on the values of the previously-treated coordinates. In practice, the displacement  
 281 of node  $i$  is iteratively limited by a factor  $\mu_i^{s_{\max}}$  as follows

$$\begin{aligned} \mathbf{d}_i^0 &= \delta_i^{[k+1]} + \boldsymbol{\xi}_i - \mathbf{x}_i^{[k]} \\ \mathbf{d}_i^{s+1} &= \begin{cases} \mu_i \mathbf{d}_i^s & \text{if } \min_{K \in \mathcal{B}_i^{[k,k+1]}} |\Omega_K| < \epsilon \\ \mathbf{d}_i^s & \text{otherwise} \end{cases} \quad \forall s \in [0, \dots, s_{\max} - 1] \\ \widetilde{\Delta \mathbf{x}}_i^{[k+1]} &= \mathbf{d}_i^{s_{\max}} \end{aligned} \quad (13) \quad \text{eq:limiter}$$

282 The limiter is thus the result of local sub-iterations, which are stopped when a  
 283 volume greater than  $\epsilon$  is guaranteed for every element in the ball. This check allows  
 284 to enforce the validity of every intermediate mesh configuration, effectively preventing  
 285 the occurrence of invalid elements at a reasonable computational cost, with respect to  
 286 smoothing or untangling procedures for unstructured meshes Hansen2004, Toulorge2013 [24, 47].

287 It must be remarked that for interior nodes in general one iteration of the above  
 288 procedure is enough, while more iterations are required when applying the limiter within

289 the projection step enforcing the boundary conditions (cf. next section). For simplicity  
 290 here the same value  $\mu_i = 0.5$  has been adopted for all the nodes. In the present work, this  
 291 value has proven to be effective in locally preventing tangling while allowing the position  
 292 of blocked nodes to be naturally relaxed by the successive application of r-adaptation  
 293 at the next time steps, as the monitor function moves with the flow.

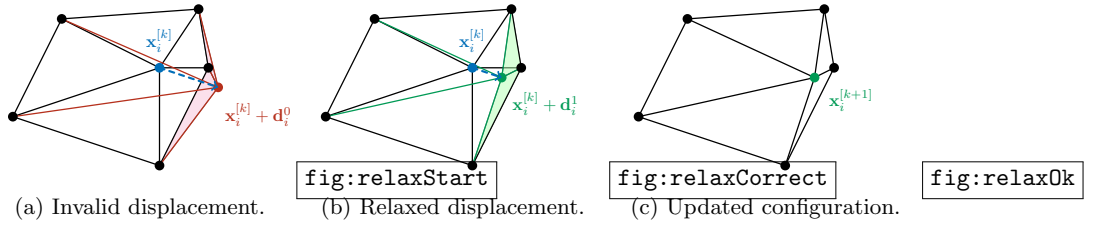


Figure 1: Two-dimensional illustration of the nodal displacement limiting. **fig:relaxStart**: Proposed displacement for node  $i$  right after the Jacobi iteration  $k + 1$ , that would produce inverted elements (in red). **fig:relaxCorrect**: Relaxed displacement producing valid elements (in green). **fig:relax0k**: Updated configuration.

**fig:relax**

**sec:slip**

### 3.4. *A-posteriori corrections on Dirichlet and slip boundaries*

295 The decoupling of the spatial coordinates obtained by initially accounting for natural  
 296 boundary conditions only is particularly convenient in terms of computational cost and  
 297 simplicity of implementation. It allows to store and assembly only a single smaller  
 298 stiffness matrix to be used for every space coordinate, instead of a matrix of  $3 \times 3$   
 299 blocks. However, the resulting nodal displacements need to be corrected to account  
 300 for conditions on Dirichlet and slip boundaries. This is achieved by the projection  
 301 step discussed in this section, which is easily embedded in the scalar iterations. The  
 302 description is given for slip wall boundaries, of which Dirichlet nodes are a particular  
 303 case.

304 In the **Fmg** library boundary geometries are handled by means of curved point-normal  
 305 triangles [51], i.e. piecewise cubic Bézier patches for the boundary position and quadratic  
 306 for the boundary normal vector, relying on the implementation provided in **Mmg** [12, 1].  
 307 In this setting an implicit surface representation of the slip boundary reading in the  
 308 continuous case

$$\gamma^S(\mathbf{x}) = 0 \quad \text{on } \Gamma_\xi^S \tag{14} \quad \text{eq:surface}$$

309 is approximated by the explicit piecewise parametric representation

$$\begin{aligned} \chi_\tau[\mathbf{x}_j, \hat{\mathbf{n}}_j] : \Sigma \rightarrow \Gamma_\xi^S, \quad \Sigma = [0, 1] \times [0, 1], \quad \Gamma_\xi^S \subset \mathbb{R}^3 \\ \mathbf{x} = \chi_\tau[\mathbf{x}_j, \hat{\mathbf{n}}_j](\mathbf{w}), \quad \mathbf{w} \in \Sigma \end{aligned} \tag{15} \quad \text{eq:model_geo}$$

310 which is defined for each triangle  $\tau$  in the triangulation of the slip boundary, from the  
 311 positions and unit normals  $\{\mathbf{x}_i, \hat{\mathbf{n}}_i\}_{i \in \tau}$  of the nodes of the triangle. Similarly, the Bézier  
 312 patches also allow to evaluate surface normals as

$$\begin{aligned} \eta_\tau[\mathbf{x}_j, \hat{\mathbf{n}}_j] : \Sigma \rightarrow \Gamma_\xi^S, \quad \Sigma = [0, 1] \times [0, 1], \quad \Gamma_\xi^S \subset \mathbb{R}^3 \\ \hat{\mathbf{n}} = \eta_\tau[\mathbf{x}_j, \hat{\mathbf{n}}_j](\mathbf{w}), \quad \mathbf{w} \in \Sigma \end{aligned} \tag{16} \quad \text{eq:model_normal}$$

313 For some applications, as for example external aerodynamics, handling curved ge-  
 314 ometries is a necessity. As a consequence, the geometric approximation becomes an  
 315 integral part of the numerical method. In particular, in three dimensions even the sim-  
 316 plest combination of boundary surfaces easily leads to intersection curves. Since sharp  
 317 edges (ridges) in the initial geometry need to be preserved as well as corners (**intersec-**  
 318 **tions of multiple ridges**), nodes cannot cross a ridge, but they are only allowed to move  
 319 tangentially to it, and displacement of a corner node cannot happen. **As outlined in sec-**  
 320 **tion 2.1, slip boundary conditions bring a position constraint expressing the belonging**  
 321 **of the node to the surface, and a null normal stress condition on the local tangent plane.**  
 322 **The latter being already fulfilled by the Neumann conditions naturally imposed on the**  
 323 **weak formulation, only the former is of our interest here. Although node belonging to an**  
 324 **intersection curve can be formally expressed as the belonging to the two surfaces sharing**  
 325 **the curve, this is not practical from an implementation point of view.** Slip boundary  
 326 conditions need thus to be specialized to the chosen geometry approximation and to  
 327 distinguish among regular curved surfaces, ridges, and corners.

328 In the following, the boundary treatment is detailed for the supported geometri-  
 329 cal features: manifold surfaces, ridges (i.e. intersections of two manifold surfaces) and  
 330 corners (intersections of two or more ridges). Note that different geometrical repre-  
 331 sentations involving other local or global manifold parametrizations can be easily embedded  
 332 in the algorithm.

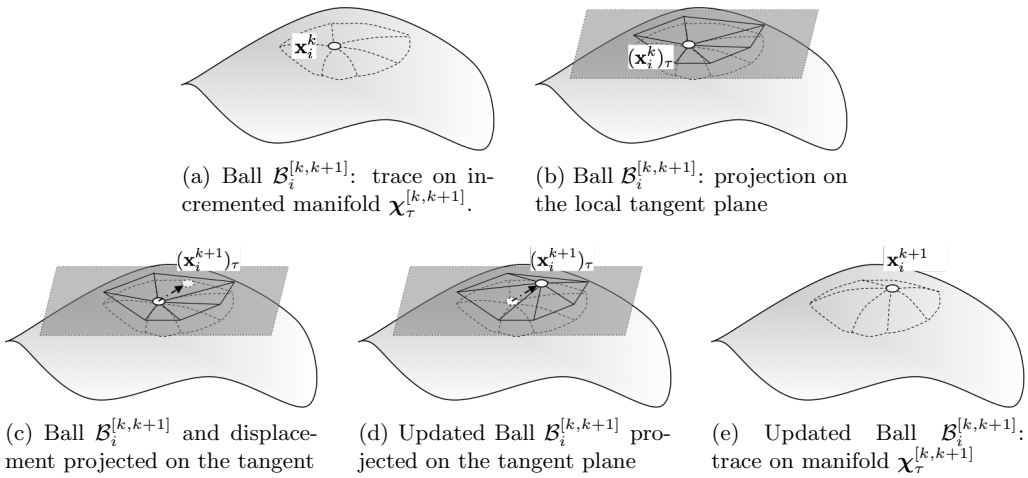


Figure 2: Illustration of the slip boundary projection procedure.

fig:mesh-proj

333 *Manifold surfaces.* The procedure adopted here to handle slip conditions along manifolds  
 334 for a node  $i$  consists in iteratively projecting the point position on the surface, updating  
 335 the Bézier patches, and limiting at the same time the displacement to ensure mesh  
 336 validity. Tangling can typically occur on surface triangles if too large displacements are  
 337 allowed, but also the adjacent volume elements can tangle when a point is projected on

338 a concave boundary. For this reason the mesh validity check is always performed on  
 339 volume elements.

340 In the first step, we work based on the partially updated ball  $\mathcal{B}_i^{[k,k+1]}$ , which allows  
 341 to build a local updated geometrical model. As before, this model is evaluated using the  
 342 new updates for nodes already processed, and value from the previous iteration for the  
 343 remaining ones. This provides the incrementally updated geometry model  $\chi_\tau^{[k,k+1]} =$   
 344  $\chi_\tau[\{\mathbf{x}_j^{[k+1]}, \hat{\mathbf{n}}_j^{[k+1]}\}_{j < i}, \{\mathbf{x}_j^{[k]}, \hat{\mathbf{n}}_j^{[k]}\}_{j \geq i}]$  (cf. [\(I5\)](#)). In particular, as shown on figures [2-\(a\)](#)  
 345 and [2-\(e\)](#), this allows to identify the trace of  $\mathcal{B}_i^{[k,k+1]}$  on the updated manifold, and its  
 346 projection on the local tangent plane.

347 The second step consists of four coupled ingredients:

- 348 1. projection of the displacement provided by the Jacobi iteration onto the local  
 349 tangent plane, leading to an approximate tangent displacement  $(\delta_i^{k+1})_\tau$ ; and pre-  
 350 liminary nodal position  $(\mathbf{x}_i^{k+1})_\tau$ , as shown on figure [2-\(c\)](#);
- 351 2. identification of the element containing the new node position, based on baricentric  
 352 coordinates interpolation, as shown on figures [2-\(c\)](#) and [2-\(d\)](#);
- 353 3. Bézier interpolation  $\chi_\tau^{[k,k+1]}(\mathbf{w})$  on the geometrical model, as shown on figure [2-\(e\)](#);
- 354 4. limiting of the displacement based on the minimum element volume, as discussed  
 355 in section [3.3](#).

356 The iterations providing the final displacement, and hence position, are similar to [\(I3\)](#):

$$\begin{aligned}
 \mathbf{d}_i^0 &= \chi_\tau^{[k,k+1]} \left( \mathbf{w}(\mathbf{x}_i^{[k+1]})_\tau \right) - \mathbf{x}_i^{[k]} \\
 \mathbf{d}_i^{s+1} &= \begin{cases} \chi_\tau^{[k,k+1]} \left( \mathbf{w}(\mathbf{x}_i^{[k]} + \mu_i \mathbf{d}_i^s) \right) - \mathbf{x}_i^{[k]} & \text{if } \min_{K \in \mathcal{B}_i^{[k,k+1]}} |\Omega_K| < \epsilon \\ \mathbf{d}_i^s & \text{otherwise} \end{cases}, \quad (17) \quad \boxed{\text{eq:relaxSlip}} \\
 \forall s &\in [0, \dots, s_{\max} - 1] \\
 \widetilde{\Delta \mathbf{x}}_i^{[k+1]} &= \mathbf{d}_i^{s_{\max}}
 \end{aligned}$$

357 We stress again that since the piecewise patches depend on both node positions and  
 358 unit normals, the position update is always accompanied by the re-evaluation of the  
 359 unit normal vectors through the analogously defined model  $\eta_\tau^{[k,k+1]}$  (cf. [\(I6\)](#)). This is  
 360 omitted from [\(I7\)](#) to keep a lighter notation.

361 *Ridges.* The displacement check and projection on boundary ridges is handled exactly  
 362 in the same way as for manifold surfaces. The main difference is that now the parametric  
 363 space is replaced with a curve parametrisation which is one-dimensional  $\Sigma \subset \mathbb{R}$ . Thus  
 364 all operations previously performed on the tangent plane are performed by projection  
 365 on the tangent line, and normal vectors of both the manifold surfaces joining at the  
 366 ridge are stored and updated in the geometrical model.

367 *Corners.* These are the only allowed Dirichlet nodes, thus corners verify exactly the  
 368 boundary condition, and are not included in the discrete variational form [3.1](#). In this

369 specific case, displacement is not allowed as they are already on the exact geometry, and  
 370 the condition imposed is

$$\mathbf{x}_i^{[k+1]} = \boldsymbol{\xi}_i \quad (18)$$

### 371 3.5. Unsteady mesh adaptation through restarted iterations

372 Following [Tang2005, Chen2008](#) [\[41, 11\]](#), dynamic mesh adaptation during the time evolution of a fluid  
 373 flow simulation is performed by repeating the steady adaptation procedure described in  
 374 the previous section at each time step, without the explicit formulation of a differential  
 375 equation in time for mesh motion. This simplifies the coupling with existing flow solvers.

376 In this case of fixed boundary domains, the reference mesh  $\boldsymbol{\xi}$  is constant in time,  
 377 while the computational mesh  $\mathbf{x}(t^{(n+1)})$  is the r-adaptation of the (fixed) reference mesh.  
 378 Thus, the displacement at each time step  $n + 1$  is initialized with the value achieved at  
 379 the last Jacobi iteration  $K$  achieved in the previous time step  $n$

$$\boldsymbol{\delta}_i^{[0](n+1)} = \boldsymbol{\delta}_i^{[K](n)} \quad (19)$$

380 so that successive Jacobi iterations during time evolution are effectively accumulated on  
 381 the nodes positions.

## 382 4. Validation via adaptation on analytical functions

383 We consider here a series of analytical tests allowing to measure the effectiveness  
 384 of the method. As shown in section [2](#), we recall here that the mesh adaptation model  
 385 can be governed by the number of iterations  $n_{it}$  plus the three parameter pairs  $(\alpha, \gamma_\alpha)$ ,  
 386  $(\beta, \gamma_\beta)$ ,  $(\tau, \gamma_\tau)$ , representing the intensity and the normalization constant of the solution  
 387 gradient, the solution Hessian, and the solution itself in the definition of the monitor  
 388 function. In this work, we have not seen specific benefits in mixing all three param-  
 389 eter pairs, so we will explicitly report only the values for the used pairs, while values  
 390 not shown are assumed to be zero. As elucidated in [Chen2008](#) [\[11\]](#), since the reference domain  
 391 Laplacian model in multiple dimensions is not derived from an error equidistribution  
 392 principle, its numerical solution until convergence is not strictly required to reach satis-  
 393 factory mesh adaptation and, in practice, a number of Jacobi iterations in the order of  
 394  $\mathcal{O}(10)$  are generally sufficient to reach the desired adaptation. The number of iterations  
 395  $n_{it}$  will be reported for each case.

396 In section [4.1](#) adaptation is performed on a steady Gaussian-like function, in order  
 397 to test the convergence order on the interpolation error. In section [4.2](#) adaptation is  
 398 performed on an unsteady analytical moving front passing over a sphere, in order to  
 399 assess the capability of the model to preserve the validity of the mesh over intersecting  
 400 curved boundaries throughout the time simulation.

### 401 4.1. Steady adaptation in a square and a cube

402 We consider the approximation of the function

$$\rho = e^{\theta\psi^2}, \quad \psi = \|\mathbf{x}\|^2 - R^2 \quad (20)$$

403 with  $\theta = 40$ ,  $R = 0.75$ . We consider both a two and three dimensional variant of the  
 404 problem, the first defined on a square domain  $[-2, 2] \times [-2, 2]$ , the second on the cube  
 405  $[-2, 2] \times [-2, 2] \times [-2, 2]$ . This solution is plotted in figures [4a](#) and [4b](#). In both cases we  
 406 consider a series of simplicial meshes with a uniform mesh size distribution, and different  
 407 average edge size  $h$ , whose details are shown in tables [1](#) and [2](#). The above function is  
 408 chosen in order to test capability of the models to adapt on a circle represented by  
 409 a smooth solution field, before their application to solutions with sharp/discontinuous  
 410 features. The mesh PDE parameters are set to  $(\tau, \gamma_\tau) = (5000, 1.0)$  in 2D, and to  
 411  $(\alpha, \gamma_\alpha) = (500, 0.1)$  in 3D. Also note that the a-posteriori limiter for the displacement is  
 412 only applied in 3D, which is the case in which tangling is more often occurring.

413 On these meshes, we measure the  $L^2$ -error convergence of the  $\mathbb{P}^1$  interpolation  $\Pi\rho$

$$\|e\|_{L^2} = \left( \int_{\Omega} |\rho - \Pi\rho|^2 d\Omega \right)^{\frac{1}{2}} \quad (21)$$

414 We plot the observed trends in figures [3a](#) and [3b](#). It can be seen that in two dimensions  
 415 it is easier to preserve, quite independently from the number of iterations  $n_{it}$  performed,  
 416 the second order convergence rate of the  $\mathbb{P}^1$  interpolation, with an error reduction for  
 417 a given number of nodes shown in table [3](#), but a high number of iterations on a coarse  
 418 mesh can actually increase the error.

419 In three dimensions, while the error on the adapted meshes is considerably lower  
 420 (table [4](#)), the number of Jacobi iterations has to be increased to preserve the second  
 421 order rate. Some adapted meshes obtained from the  $h = 0.1$  and  $h = 0.05$  initial  
 422 meshes are visualized in figures [4](#) to help understand these two phenomena. Taking  
 423 as example the three-dimensional case, as the initial mesh is refined from  $h = 0.1$  to  
 424  $h = 0.05$  in figure [4](#), it can be appreciated that the displacement produced by the  
 425 same number of iterations and the same adaptation parameters is smaller. This has  
 426 two consequences. The first consequence is that a high number of iterations on coarse  
 427 meshes can excessively stretch the mesh elements (as shown in figure [4g](#)) in an orthogonal  
 428 pattern, due to the uncoupling of the Laplacian model in the coordinate directions,  
 429 possibly increasing the approximation error on the adapted mesh (as seen in table [3](#)  
 430 for the 2D case for the coarsest meshes). The second consequence is that more iterations  
 431 are needed on fine meshes to preserve the second order rate, as shown in figure [3b](#). In  
 432 three dimensions, the a-posteriori limiter also contributes to this effect by constraining  
 433 the allowed displacement of each node inside its ball at each iteration.

434 These effects can be appreciated by observing the trend for the tetrahedron quality

$$Q = \frac{\left( \sum_{j=1}^6 l_j^2 \right)^{3/2}}{\alpha |\Omega_K|} \quad (22)$$

435 where  $l_j$  is the length of each edge of the element,  $|\Omega_K|$  its volume, and  $\alpha$  the normal-  
 436 ization factor to get  $Q = 1$  on a regular tetrahedron with unit edges. Since r-adaptation  
 437 inevitably introduces some anisotropy which is not taken into account in our quality  
 438 measure, we expect the quality to be somewhat degraded in the adapted regions. Any-  
 439 way, a too high percentage of bad quality elements, when sharp solution fronts are quite

$h$	0.0125	0.025	0.05	0.075	0.1	0.15
Nb. of nodes	135550	34310	8560	3993	2213	1015
Nb. of elements	271098	68618	17118	7984	4424	2028

Table 1: Mesh data for the 2D square convergence analysis.

$h$	0.0375	0.05	0.075	0.1	0.15
Nb. of nodes	319830	140264	44521	20604	6727
Nb. of elements	1844811	802080	237458	106130	32308

Table 2: Mesh data for the 3D cube convergence analysis.

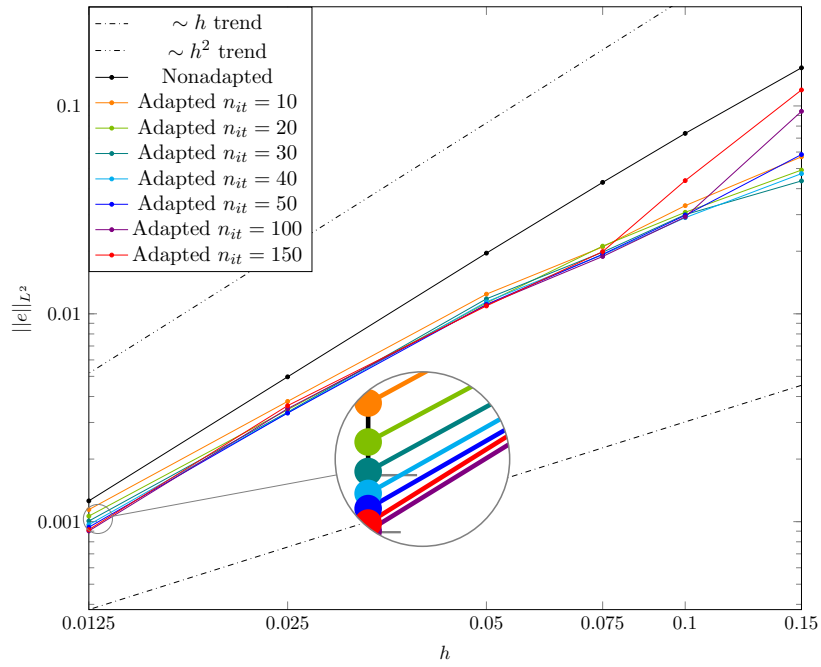
$h$	$\mathcal{E}^{[0]}$	$\mathcal{E}^{[10]}$	$r^{[10]}$	$\mathcal{E}^{[150]}$	$r^{[150]}$
0.15	1.525974e-01	5.693340e-02	62.6905 %	1.194055e-01	21.751 %
0.1	7.379553e-02	3.313339e-02	55.1011 %	4.372964e-02	40.742 %
0.075	4.288518e-02	2.097308e-02	51.0948 %	1.991813e-02	53.555 %
0.05	1.958636e-02	1.243068e-02	36.5340 %	1.090836e-02	44.306 %
0.025	4.974168e-03	3.788809e-03	23.8303 %	3.614722e-03	27.330 %
0.0125	1.258864e-03	1.142442e-03	9.2482 %	9.152757e-04	27.294 %

Table 3: Interpolation errors  $\mathcal{E}^{[k]} = \|e^{[k]}\|_{L^2}$  for the 2D square convergence analysis, for 10 and 150 iterations, and reduction  $r^{[k]} = (1 - \mathcal{E}^{[k]}/\mathcal{E}^{[0]})$  with respect to the nonadapted case.

$h$	$\mathcal{E}^{[0]}$	$\mathcal{E}^{[10]}$	$r^{[10]}$	$\mathcal{E}^{[150]}$	$r^{[150]}$
0.15	3.023667e-01	1.693936e-01	43.9774 %	1.450969e-01	52.013 %
0.1	1.533983e-01	9.494413e-02	38.1061 %	5.919961e-02	61.408 %
0.075	1.036390e-01	7.284977e-02	29.7082 %	2.832881e-02	72.666 %
0.05	4.687948e-02	4.084946e-02	12.8628 %	1.424675e-02	69.610 %
0.0375	2.671484e-02	2.499870e-02	6.4239 %	9.579343e-03	64.142 %

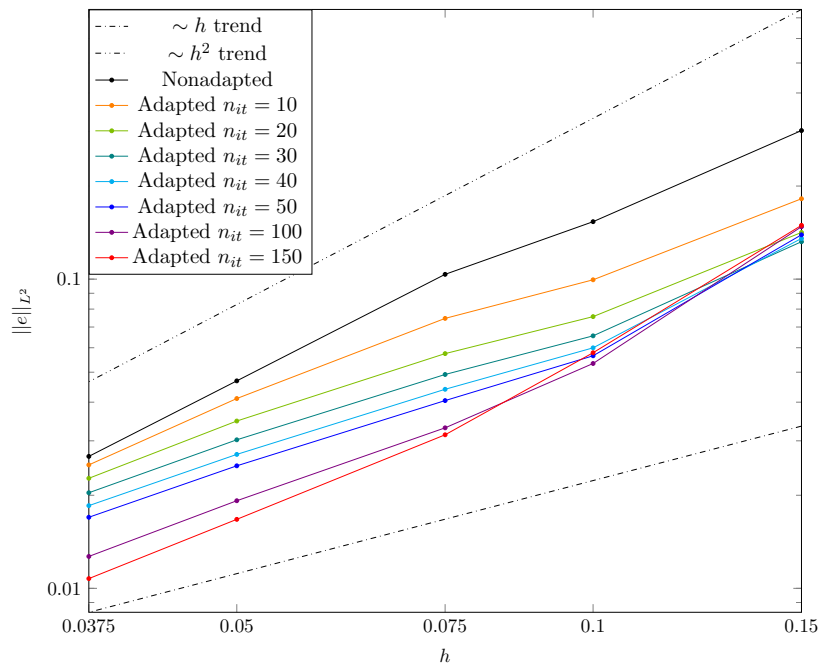
Table 4: Interpolation errors  $\mathcal{E}^{[k]} = \|e^{[k]}\|_{L^2}$  for the 3D cube convergence analysis, for 10 and 150 iterations, and reduction  $r^{[k]} = (1 - \mathcal{E}^{[k]}/\mathcal{E}^{[0]})$  with respect to the nonadapted case.

440 localized in the domain, can be a sign that the mesh is stretched also in smooth solution  
441 regions, possibly worsening the error reduction performances. In figure 5 we plot the  
442 evolution of the histograms of the elements quality with the number of iterations for the  
443  $h = 0.1$  and  $h = 0.05$  meshes. The excessive stretch observed in figure 4g corresponds to  
444 a significantly degradation of the elements quality for the  $h = 0.1$  mesh, especially when  
445 increasing the number of iterations, with more than 24% of elements having  $Q < 0.2$  for  
446 150 iterations, much higher than for the  $h = 0.05$  (less than 10%).



(a) Interpolation error trend for the 2D square test case.

fig:ErrorTrend2DConv



(b) Interpolation error trend for the 3D cube test case.

fig:ErrorTrend3DConv

Figure 3: Interpolation error convergence with mesh adaptation for the square and cube analytical test cases.

fig:convergence



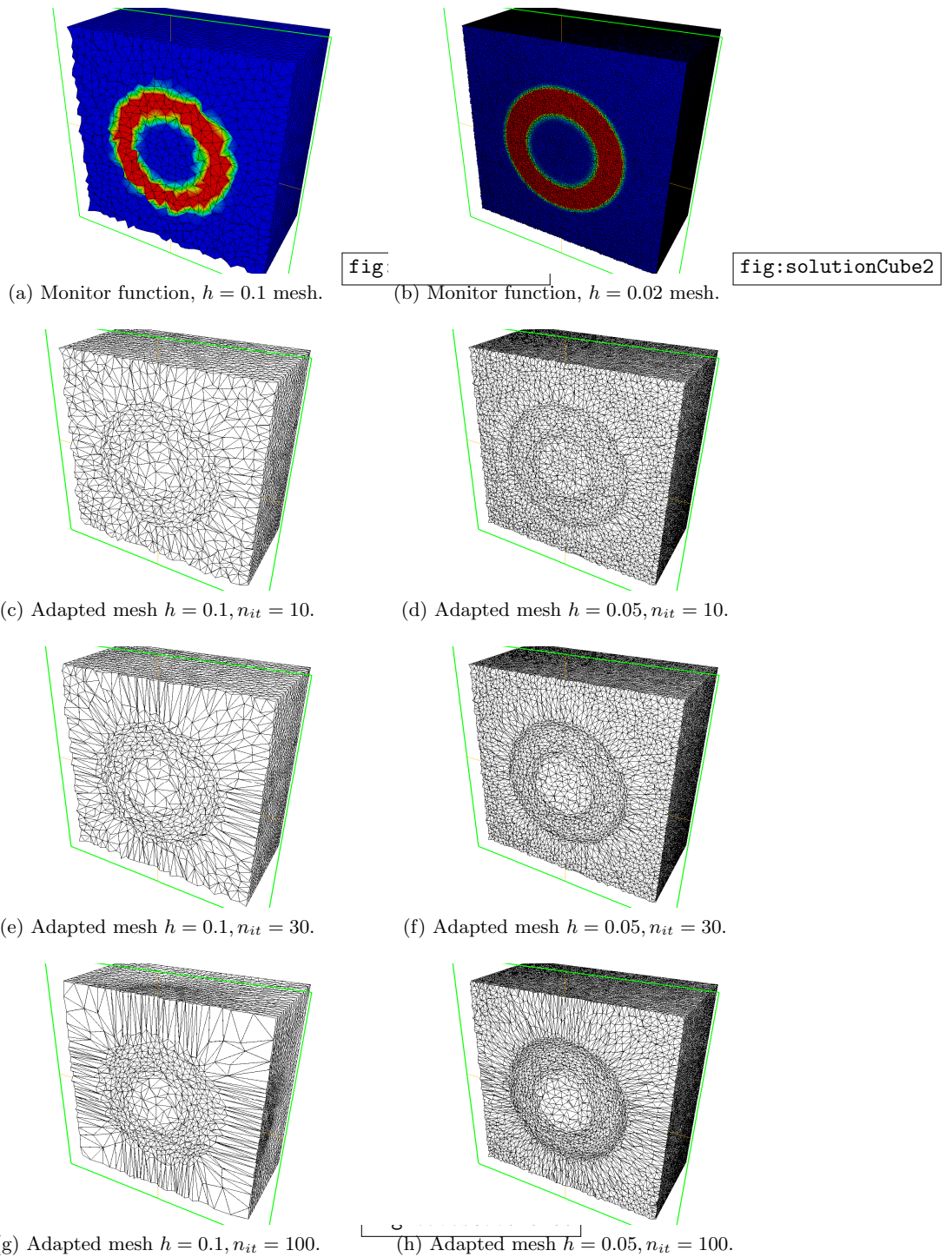


fig:cubesCut

Figure 4: Monitor function (top row) and volumic cuts in the adapted meshes (second to last row) for the cube test case, for different number of iterations, on the  $h = 0.1$  and  $h = 0.05$  initial meshes.

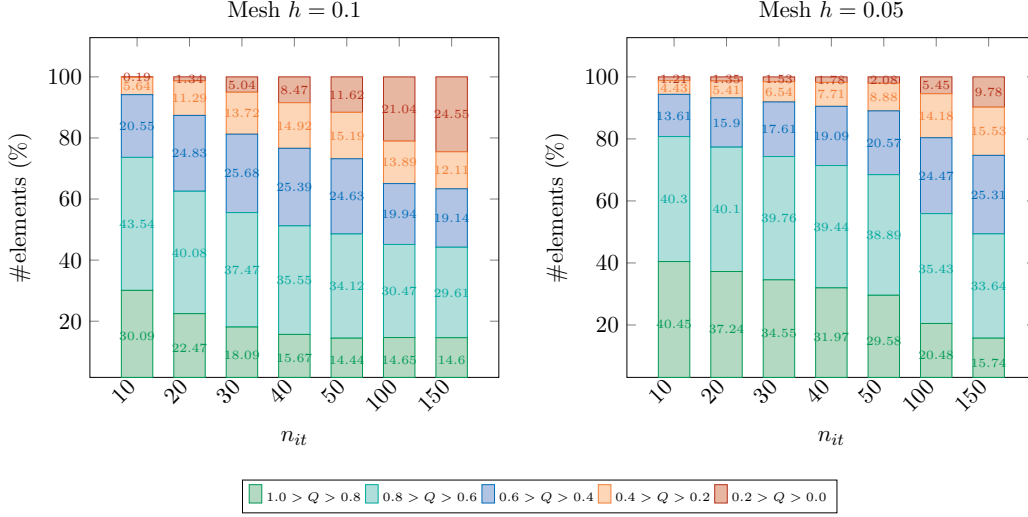


Figure 5: Evolution of mesh elements quality  $Q$  with the number of iterations  $n_{it}$  for the 3D cube test, for the  $h = 0.1$  and  $h = 0.05$  meshes.

fig:quality

sec:shockAn

447  
448

#### 4.2. Moving front passing over a spherical boundary

The algorithm was tested by adapting over a moving front defined as

$$\rho(X(x, t)) = \begin{cases} 1 & \text{if } X(x, t) < 0 \\ 0.5 \cos(s\pi X(x, t) + 1) & \text{if } X(x, t) \in [0, \delta] \\ 0 & \text{if } X(x, t) > \delta \end{cases} \quad (23)$$

449 with

$$X(x, t) = s(x - x_0 + vt) \quad (24)$$

450 and scaling  $s = 20$ , initial position  $x_0 = 0.7$ , speed  $v = 0.2$ , front thickness  $\delta = 0.005$ .  
451 Unsteady mesh adaptation is performed on this analytical solution every  $\Delta t = 0.25$ .

452 The setup is shown in figures 6a and 6b. The domain is a quarter cylinder of radius  
453 1.5 along the x-axis with  $x \in [-1.5, 1.5]$ , surrounding a quarter sphere centered at the  
454 origin with radius 0.5. This case is designed to test as many geometrical sources of mesh  
455 tangling as possible before the application to fluid flow simulations, as it contains at the  
456 same time curved surfaces, ridges (the intersection of the sphere with each symmetry  
457 planes) and corners (the intersections of the sphere with both the symmetry planes),  
458 and a sharp solution moving over the geometry. Adaptation is performed with  $(\alpha, \gamma_\alpha) =$   
459  $(40, 0.1)$ , with 30 Jacobi iterations, on an uniform mesh with edge size  $h = 0.05$ . The  
460 number of nodes and elements is reported in table 5, as this is the same base mesh that  
461 will be used for the shock-sphere interaction simulations in the next section.

462 The obtained meshes are shown in figure 6 showing in particular that the method  
463 is able to preserve a valid mesh both when the front is passing over the surface of  
464 the sphere (figures 6e, 6f) and most importantly when it hits and leaves the sphere

465 (figures [6c](#), [6d](#) and [6g](#), [6h](#) respectively). Without the a-posteriori limiter, that effectively  
 466 blocks excessive deformation near the corners and in the first layer of elements above  
 467 the curved surface, it was impossible to complete the simulation without the occurrence  
 468 of tangled elements.

469 *Remarks on mesh folding and the purpose of the a-posteriori limiter.* As discussed in  
 470 section [I](#), there is no analytical proof for the validity of the meshes produced by our  
 471 model neither in the continuum nor in the discrete setting. Examples of folded meshes  
 472 have indeed already been reported in the literature for several other methods [\[15, 31\]](#).  
 473 Mesh folding has not been reported for the variable-diffusion Laplacian in the reference  
 474 domain in two dimensions [\[10, 40, 11\]](#), but in [\[10\]](#) the authors themselves remark that  
 475 there is no theoretical reason against its occurrence. In three dimensions, we have  
 476 found that it is quite frequent to produce folded elements for too strong adaptation  
 477 parameters or on concave boundaries when the limiter presented in the previous section  
 478 is not applied. An example of the first situation is given in figure [7a](#), where an inverted  
 479 element is produced just outside of the most refined region. An example of tangling on a  
 480 concave boundary is given in figure [7b](#), where two points on the surface are blocked and  
 481 cannot move without folding the adjacent elements (the volume limiter is not applied,  
 482 but displacement on the surface is limited on the surface ball in order to allow the  
 483 projection on Bézier patches), and one element near the lower circle is folded.

484 In the numerical simulations presented in the next section, all of which have con-  
 485 cave boundaries, tangling was observed whenever a shock wave hit or developed on the  
 486 front of the object, without limiter. Since this happened in the first **instants** of the  
 487 simulations, we have found that the straightforward three-dimensional extension of the  
 488 original variable-diffusion Laplacian method in the reference domain [\[10\]](#) would simply  
 489 be unpractical on those cases without an additional limiting or correction step to avoid  
 490 mesh folding.

## 491 5. Adaptation for unsteady compressible flows

`sec:FlowRes`

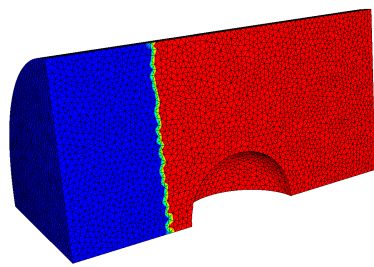
492 We consider the simulation of unsteady inviscid compressible flows in a time dependent  
 493 frame of reference. In particular, we couple the `Fmg` library we developed to the  
 494 `Flowmesh` solver [\[22, 29, 38\]](#), based on a node-centered second order, total variation-  
 495 diminishing finite volume scheme for the Euler equations, written in an Arbitrary-  
 496 Lagrangian-Eulerian (ALE) form [\[13\]](#)

$$\frac{d}{dt} \int_{\Omega(t)} \mathbf{u} \, d\Omega + \oint_{\partial\Omega(t)} \hat{\mathbf{n}} \cdot (\mathbb{F}(\mathbf{u}) - \mathbf{v}\mathbf{u}) \, d\Gamma = \mathbf{0} \quad (25)$$

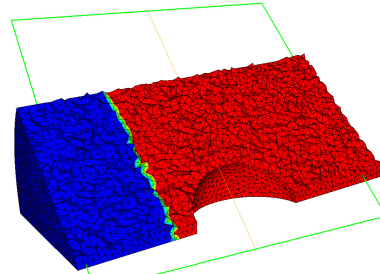
`eq:solvALE`

497 where  $\mathbf{u}$  is the array of the conservative solution,  $\mathbb{F}(\mathbf{u})$  its flux,  $\rho$  denotes the mass  
 498 density,  $\rho\mathbf{U}$  the momentum, and  $\rho e^t$  the total energy density. The moving domain  
 499 velocity is represented by the vector field  $\mathbf{v}$

$$\mathbf{u} = \begin{pmatrix} \rho \\ \rho\mathbf{U} \\ \rho e^t \end{pmatrix}^T, \quad \mathbb{F}(\mathbf{u}) = \begin{pmatrix} \rho\mathbf{U} \\ \rho\mathbf{U} \otimes \mathbf{U} + P\mathbb{I} \\ \rho e^t\mathbf{U} + P\mathbf{U} \end{pmatrix}^T \quad (26)$$

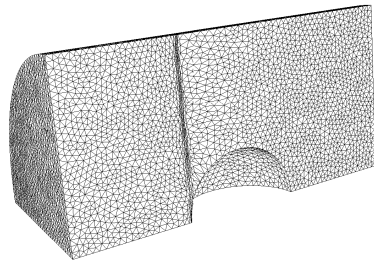


(a) Solution on input mesh boundary.

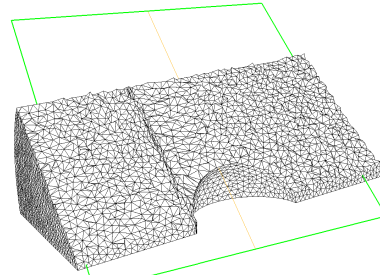


(b) Solution on input mesh volumic cut.

fig:FrontInputCut

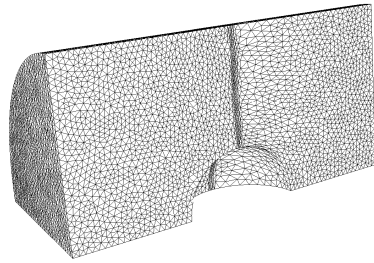


(c) Output mesh boundary at  $t = 1.0$ .

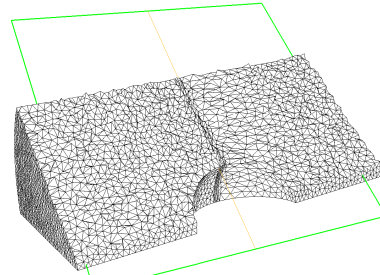


(d) Output mesh volumic cut at  $t = 1.0$ .

fig:FrontHitCut

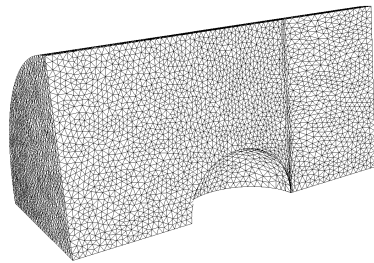


(e) Output mesh boundary at  $t = 3.5$ .

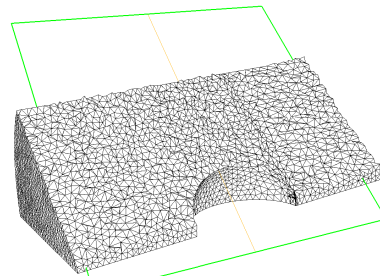


(f) Output mesh volumic cut at  $t = 3.5$ .

fig:FrontTopCut



(g) Output mesh boundary at  $t = 6.0$ .

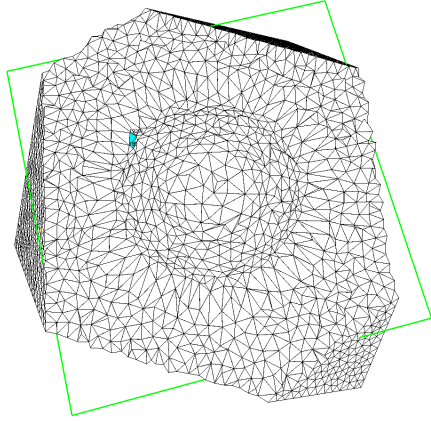


(h) Output mesh volumic cut at  $t = 6.0$ .

fig:FrontLeaveCut

fig:MovingFront

Figure 6: Moving front test case, meshes from  $t = 0.0$  to  $t = 6.0$ .



(a) Cube  $h = 0.1$  fifth iteration without limiter with  $(\tau, \gamma_\tau) = (10000, 0.1)$ . One inverted element (cyan).

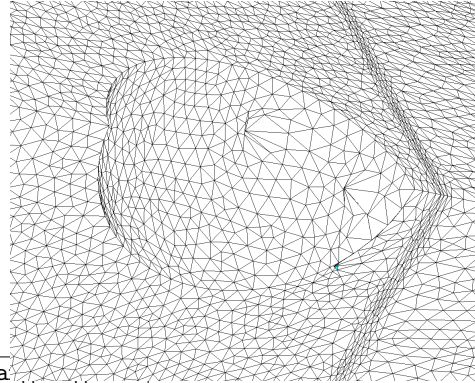


fig:Tan

(b) Moving front test case without limiter at  $t = 6.5$ . Two blocked points (distorted balls on the surface of the sphere) and one inverted element near the lower circle (cyan).

fig:TanglingSphere

fig:Tangling

Figure 7: Examples of folded meshes with no limiter applied.

The pressure  $P$  is computed using the ideal gas equation of state for ideal gases

$$P = (\gamma - 1) \left( \rho e^t - \frac{1}{2} \rho |\mathbf{U}|^2 \right)$$

500 Within the code, a local conservative solution transfer procedure at each time step is  
 501 guaranteed by the ALE formulation.

502 Unsteady mesh adaptation is performed according to the scheme shown in section [3.5](#). [eq:r:adaptDyn](#)  
 503 At each time step, the flow solution is predicted on the previous computational mesh,  
 504 then the computational mesh is adapted, and finally the flow solution is recomputed  
 505 on the adapted mesh. To this end, `Flowmesh` makes use of a conservative ALE-remap  
 506 exactly matching the volumes swept by cell faces during mesh displacements and nodal  
 507 volumes, and automatically fulfilling a Discrete Geometric Conservation Law (DGCL)  
 508 [\[23, 18, 54\]](#). The code also includes the support of topological mesh modifications like  
 509 edge split, edge collapse, barycentric node insertion, and Delauney node insertion, not  
 510 used in this work.

511 To apply mesh adaptation at each time step, a low order computation of the solution  
 512 at the next time step on the current mesh is used to provide a monitor function to the  
 513 mesh PDEs.

#### 514 5.1. Case 1: two-dimensional forward facing step

515 As a preliminary validation, we reproduce the results shown for the same method  
 516 without a posteriori relaxation in [\[11\]](#) for the two-dimensional forward facing step [\[17,](#)  
 517 [50, 53\]](#). Our initial mesh is a Delauney triangulation made of 10946 elements, 5474  
 518 nodes, with an average edge length  $h = 0.0025$ . Note that this unstructured mesh has

	Base mesh		Refined mesh	
	# nodes	# elements	# nodes	# elements
Step 2D	5474	10946	21639	43276
Step 3D	47445	277655	555026	3217351
Shock-sphere	35379	209142	488963	2872845

Table 5: Number of nodes and elements for the simplicial meshes employed for the unsteady compressible flow cases.

tab:MeshDataFlow

	Base (nonadapted)	Base (adapted)	Refined (nonadapted)
Step 2D	31m 32s	44m 43s	2h 52m 21s
Step 3D	1h 39m 55s	2h 21m 28s	45h 37m 18s
Shock-sphere	40m 12s	1h 32m 48s	12h 5m 12s

Table 6: Computational times comparison. The overhead due to solution prediction and adaptation is important, but negligible if compared with an uniform refinement strategy.

tab:MeshTimeFlow

519 a higher edge size with respect to the one proposed in [WoodwardColella1984](#)  
520 [\[53\]](#), which had an edge size  
521  $h = 0.00125$ . The initial condition is a uniform Mach 3 flow towards the right of the domain.

522 All simulations are run on 4 cores of a Intel Xeon E5-2690 (2.6 GHz), mesh adaptation  
523 is serial. We perform mesh adaptation on the base  $h = 0.0025$  mesh, and compare results  
524 with those obtained without adaptation on the refined  $h = 0.00125$  mesh. Adaptation  
525 is performed on mass density, with  $(\alpha, \gamma_\alpha) = (40, 0.1)$  and  $(\beta, \gamma_\beta) = (10, 0.5)$ . Mesh  
526 data are shown in table [5](#), while contour lines for mass density are compared in figures [8](#)  
527 and [10](#). Contour lines range and spacing for each time instant is the same as in [\[53\]](#).  
528 The adapted meshes are shown in figures [9](#) and [11](#). Shock waves are resolved better  
529 on the coarse adapted mesh than on the refined nonadapted mesh, while resolution on  
530 rarefaction fans and contact discontinuities is comparable. Computational times are  
531 shown in table [6](#). While mesh adaptation produces a significant overhead if compared  
532 to the base nonadapted case, this overhead is negligible if compared to the refined  
533 nonadapted calculation.

## 534 5.2. Case 2: three-dimensional forward facing step

535 We propose a three-dimensional extension of the classical supersonic forward facing  
536 step. The impulsive start of a Mach 3 flow in a 3 length units long and 1 length unit  
537 wide/high wind tunnel, with a 0.2 length unit wide/high step located at 0.6 length units  
538 from the inlet (see figure [12a](#)). Adaptation is performed on the mass density (figures [12b](#)  
539 and [12c](#)), with  $(\alpha, \gamma_\alpha) = (40, 0.02)$  on a base mesh with an overall edge size  $h = 0.04$   
540 (slightly refined on the step front plane,  $h = 0.02$ ). Results are compared with those  
541 obtained without adaptation on a refined mesh with uniform edge size  $h = 0.015$ . The  
542 number of elements and nodes in the meshes are shown in table [5](#). Contour lines for  
543 mass density on the same diagonal cut plane are shown in figures [13](#) and [15](#), for 50  
544 equispaced lines between the values 0.715867 and 6.03154. To obtain a comparable  
545 resolution on shocks between the coarse adapted and the refined nonadapted meshes,

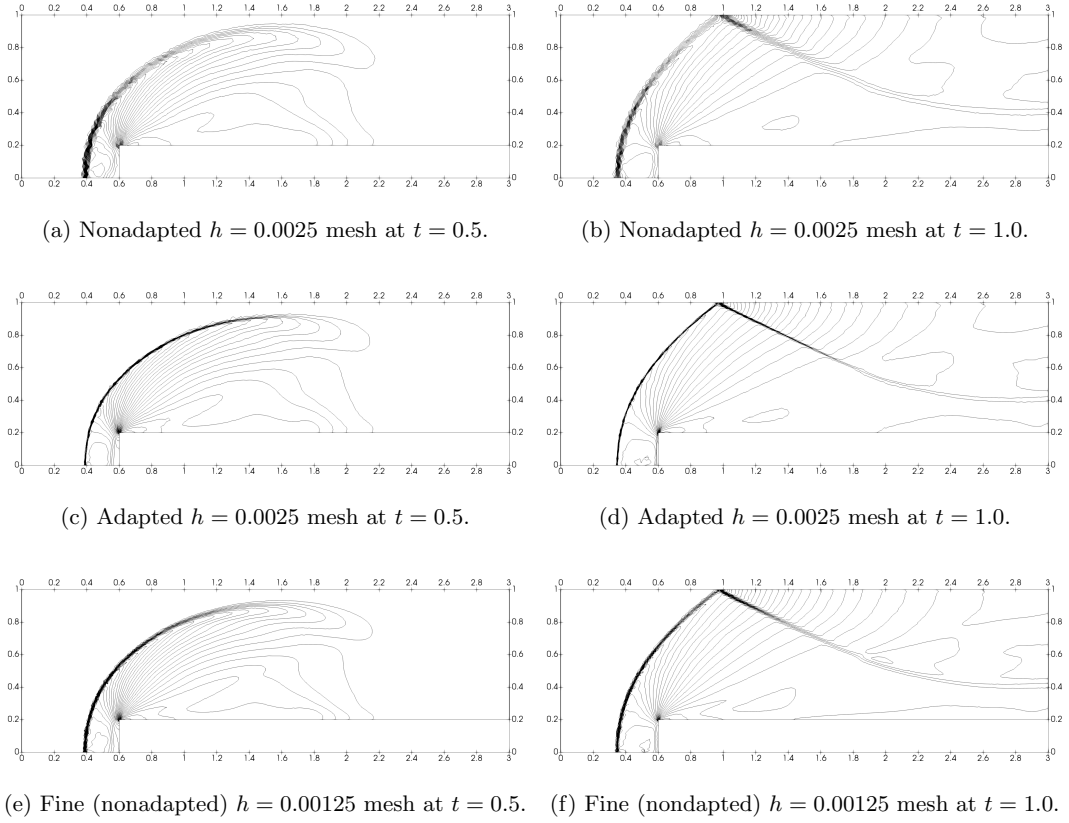


Figure 8: Two-dimensional forward facing step mass density contour lines at  $t = 0.5$  and  $t = 1.0$ .

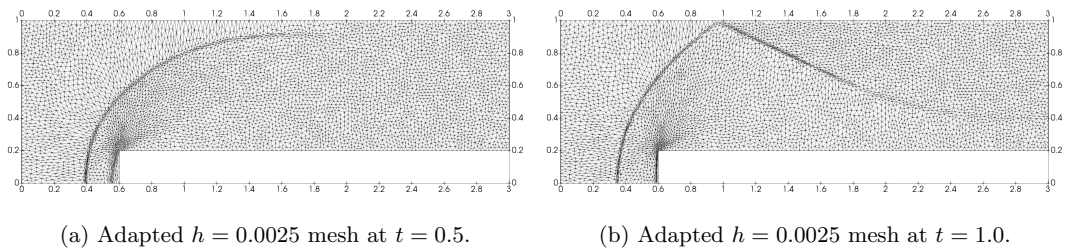


Figure 9: Two-dimensional forward facing step adapted meshes at  $t = 0.5$  and  $t = 1.0$ .

fig:contour\_t100

fig:mesh\_t100

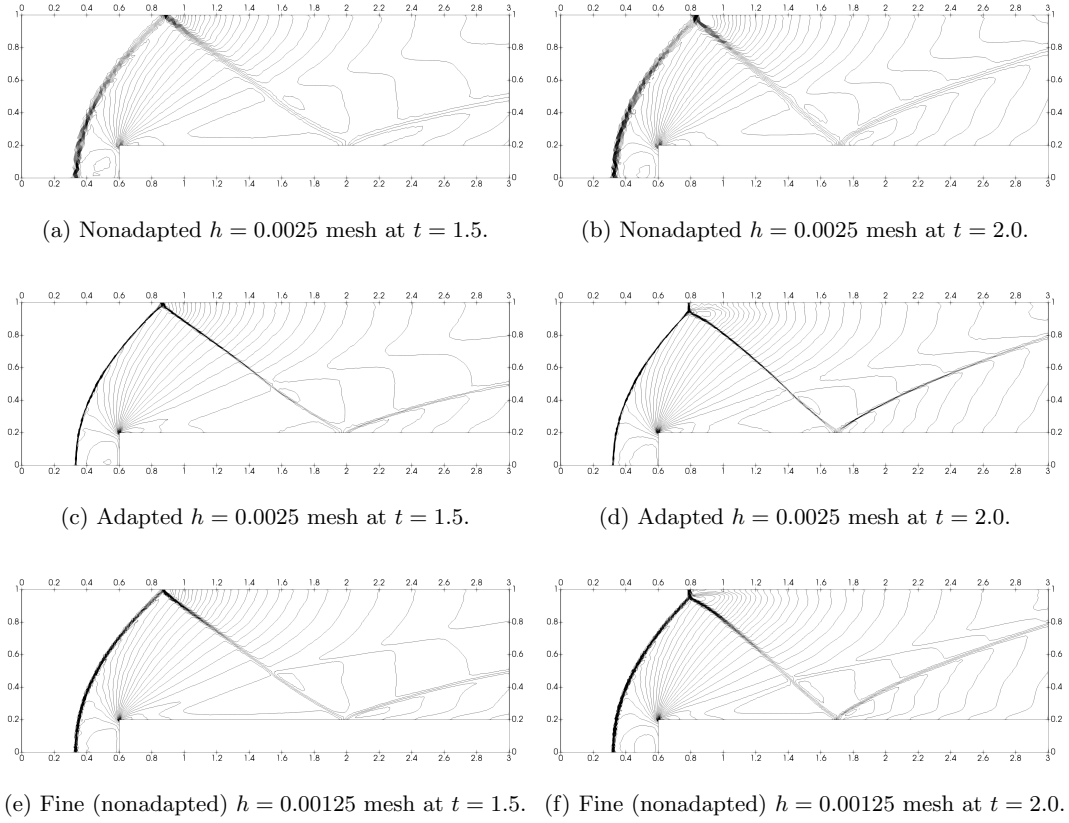


Figure 10: Two-dimensional forward facing step mass density contour lines at  $t = 1.5$  and  $t = 2.0$ .

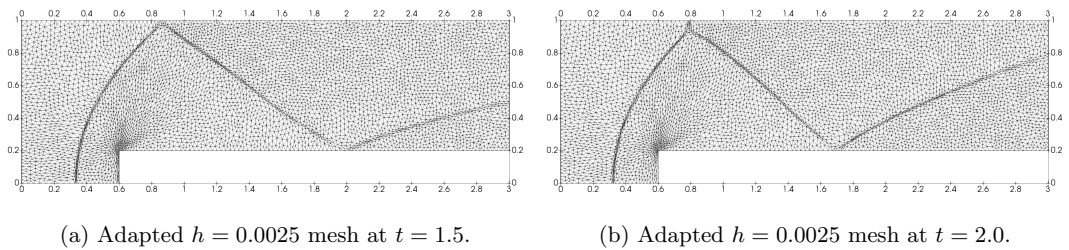
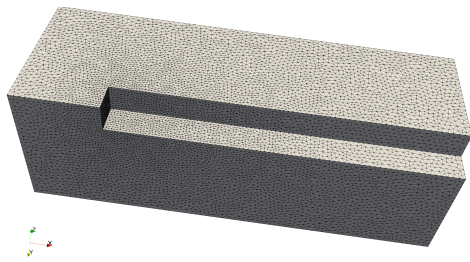


Figure 11: Two-dimensional forward facing step adapted meshes at  $t = 1.5$  and  $t = 2.0$ .

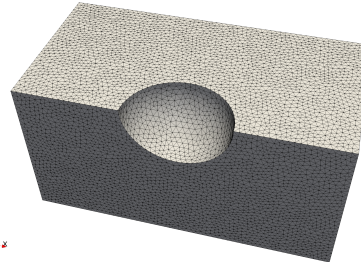
fig:contour\_t200

fig:mesh\_t200



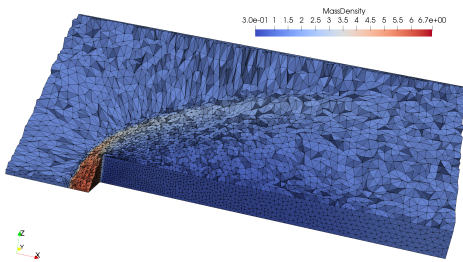


(a) Forward facing step test case.

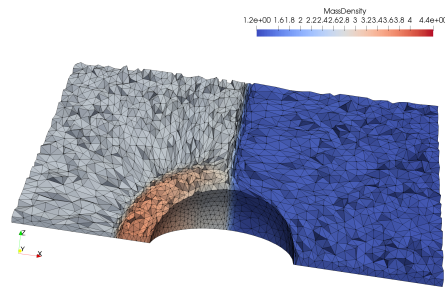


(b) Shock-sphere test case.

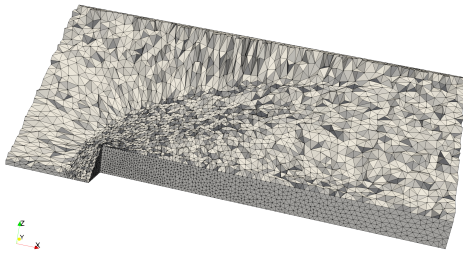
fig:gridinitsphere



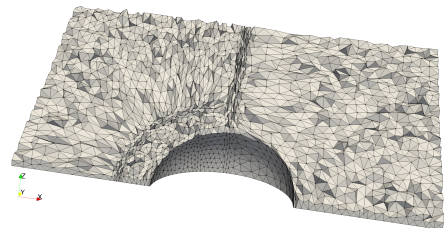
(c) Step, volumic cut and mass density at  $t = 0.7$ .



(d) Sphere, volumic cut and mass density at  $t = 90$ .



(e) Step, volumic cut at  $t = 70$ .



(f) Sphere, volumic cut at  $t = 90$ .

Figure 12: Initial meshes, adapted meshes and solution for the three-dimensional forward facing step and shock-sphere interaction cases.

fig:3dcases

546 we had to produce a refined mesh that is more than ten times bigger (in terms of nodes  
 547 and elements) than the coarse one. Note that the diagonal cut is possibly the most  
 548 demanding plane on which results can be compared, as the Laplacian model is uncoupled  
 549 in multiple space directions, thus it tends to provide better results on cartesian planes, as  
 550 shown in section 4.1. Adapted meshes are shown in figures 14 and 16. Computational  
 551 times are shown in table 6. The benefits in terms of computational times in three  
 552 dimensions are greater than in two dimensions. Anyway, while in two dimension we  
 553 observed that mesh tangling was a rare occurrence with our Laplacian model, in three  
 554 dimensions it was impossible to continue the time simulation without the a-posteriori  
 555 limiter after the first few time steps, due to the strong deformation that quickly led to  
 556 tangled elements at the step front and around its corners, but also at the shock reflection  
 557 lines.

### 558 5.3. Case 3: shock–sphere interaction

559 In order to test the capabilities of the method to handle simultaneously shock waves  
 560 and curved boundary, we choose to simulate the interaction of a traveling shock wave  
 561 on a sphere. Some configurations for the diffraction of shock waves over cylindrical,  
 562 and spherical obstacles have been studied experimentally for example in [8, 42]. An  
 563 early application of unstructured mesh adaptation to two-dimensional shock-cylinder  
 564 simulations can be found in [14], while structured grid adaptation on axisymmetric  
 565 shock-sphere simulations can be found in [39].

566 The simulation is limited to a quarter of a cylindrical domain (as for the analyti-  
 567 cally moving shock of the previous section, see figure 12b). We choose a planar shock  
 568 moving at  $M_s = 1.5$ . Adaptation is performed on the mass density (figures 17 and 19),  
 569 with  $(\alpha, \gamma_\alpha) = (40, 0.1)$ . Again, the aim is to compare the results obtained with mesh  
 570 adaptation on a base mesh with edge size  $h = 0.05$  with those obtained on a uniformly  
 571 refined mesh with edge size  $h = 0.02$ . Mesh data are shown in table 5. Contour lines  
 572 for the mass density solution on a radial plane are shown in figures 17 and 19, for 50  
 573 equispaced lines between the values 1.36081 and 4.00883. Resolution on shock waves  
 574 with mesh adaptation is comparable with those obtained on a uniform mesh about ten  
 575 times bigger in terms of number of nodes and elements. Adapted meshes are shown in  
 576 figures 18 and 20. Computational times are shown in table 6.

577 In this case too it was impossible to complete the simulation over valid meshes  
 578 without the action of the a-posteriori limiter near the corners and the curved surface.

## 579 6. Conclusions

580 The proposed algorithm for dynamic r-adaptation extends to three dimensions the  
 581 method first proposed in [10, 11, 6] for two-dimensional flows. An iterative solver based  
 582 on diagonal Jacobi iterations for the discretized mesh PDEs with natural boundary con-  
 583 ditions allows a cheap, uncoupled solution in each space direction. A novel a-posteriori  
 584 relaxation scheme allows to prevent mesh tangling through the construction of a se-  
 585 quence of valid meshes also over curved boundary surfaces and corners, which is the  
 586 main concern of r-adaptation methods in multiple dimensions, and it is interleaved with

sec:Conclusions

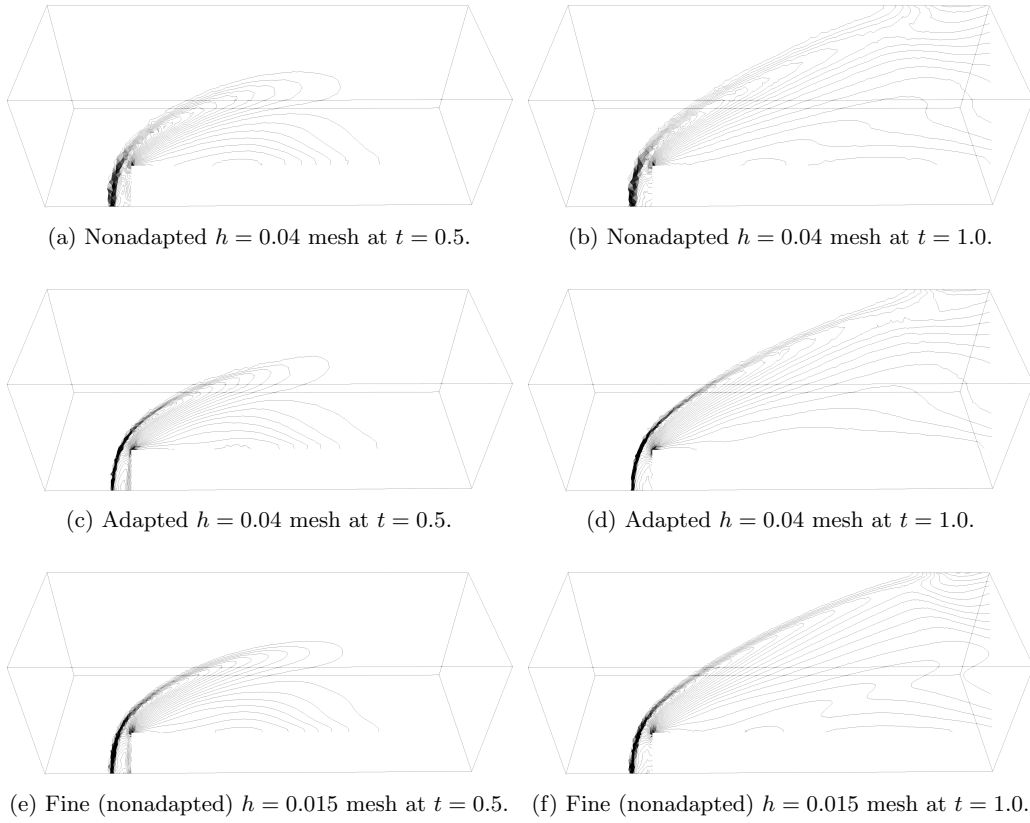


Figure 13: Three-dimensional forward facing step mass density contour lines at  $t = 0.5$  and  $t = 1.0$ .

fig:contourstep1

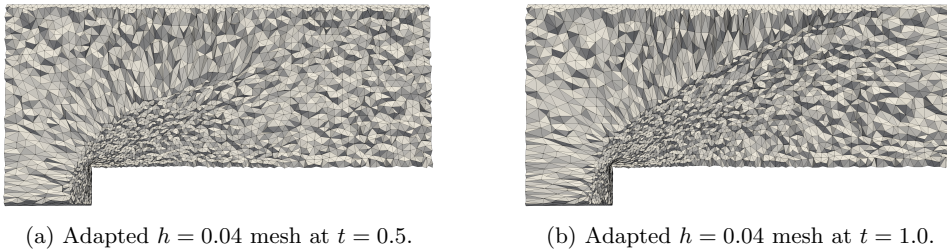


Figure 14: Three-dimensional forward facing step adapted meshes at  $t = 0.5$  and  $t = 1.0$ .

fig:meshstep1

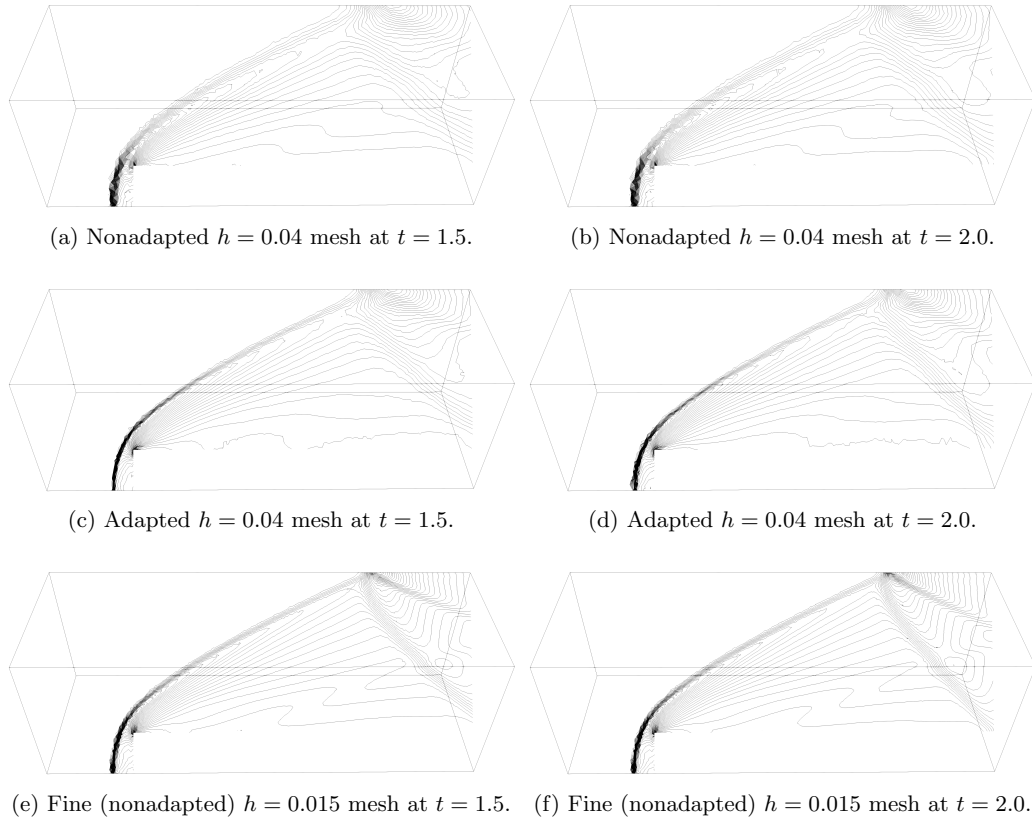


Figure 15: Three-dimensional forward facing step mass density contour lines at  $t = 1.5$  and  $t = 2.0$ .

fig:contourstep2

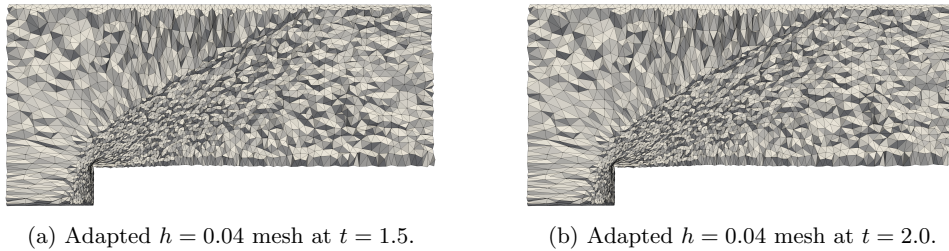
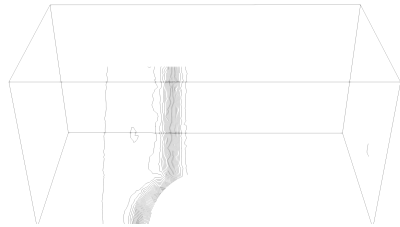
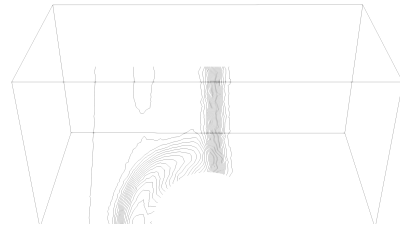


Figure 16: Three-dimensional forward facing step adapted meshes at  $t = 1.5$  and  $t = 2.0$ .

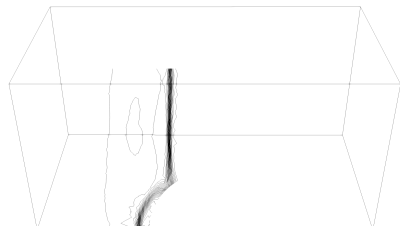
fig:meshstep2



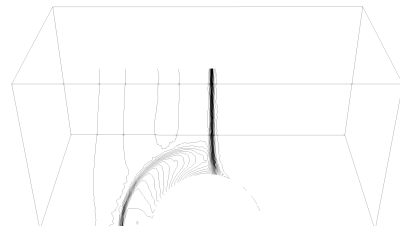
(a) Nonadapted  $h = 0.05$  mesh at  $t = 0.5$ .



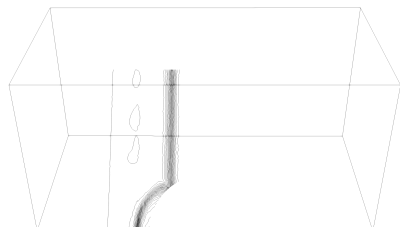
(b) Nonadapted  $h = 0.05$  mesh at  $t = 1.0$ .



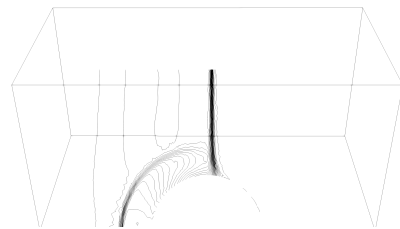
(c) Adapted  $h = 0.05$  mesh at  $t = 0.5$ .



(d) Adapted  $h = 0.05$  mesh at  $t = 1.0$ .



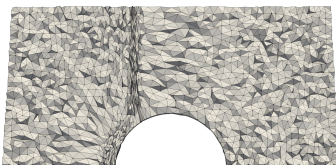
(e) Fine(nonadapted)  $h = 0.02$  mesh at  $t = 0.5$ .



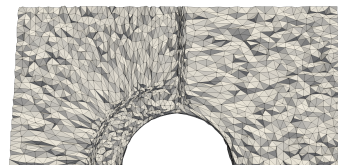
(f) Fine (nonadapted)  $h = 0.02$  mesh at  $t = 1.0$ .

g:contoursphere1

Figure 17: Shock-sphere interaction mass density contour lines at  $t = 0.5$  and  $t = 1.0$ .



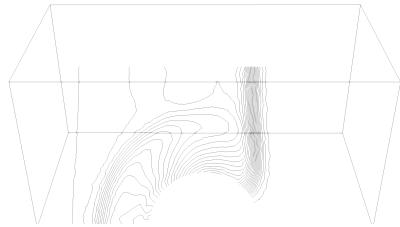
(a) Adapted  $h = 0.05$  mesh at  $t = 0.5$ .



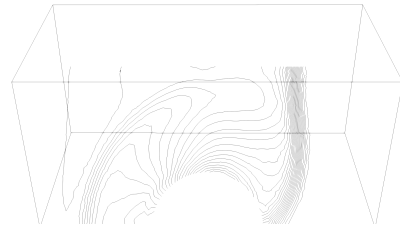
(b) Adapted  $h = 0.05$  mesh at  $t = 1.0$ .

fig:meshsphere1

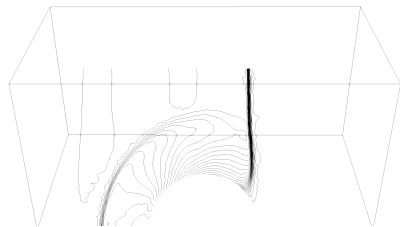
Figure 18: Shock-sphere interaction adapted meshes at  $t = 0.5$  and  $t = 1.0$ .



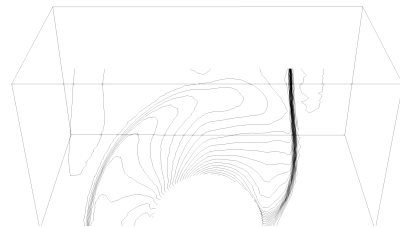
(a) Nonadapted  $h = 0.05$  mesh at  $t = 1.5$ .



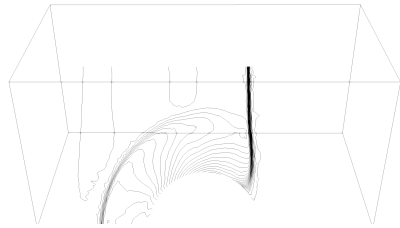
(b) Nonadapted  $h = 0.05$  mesh at  $t = 2.0$ .



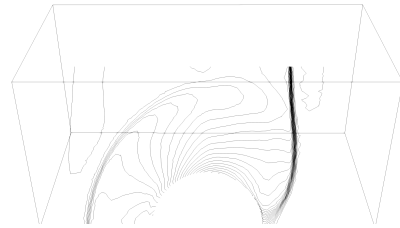
(c) Adapted  $h = 0.05$  mesh at  $t = 1.5$ .



(d) Adapted  $h = 0.05$  mesh at  $t = 2.0$ .



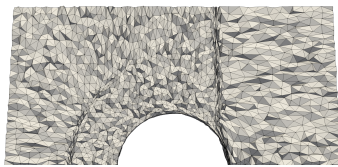
(e) Fine (nonadapted)  $h = 0.02$  mesh at  $t = 1.5$ .



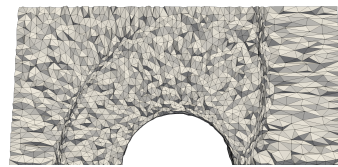
(f) Fine (nonadapted)  $h = 0.02$  mesh at  $t = 2.0$ .

g:contoursphere2

Figure 19: Shock-sphere interaction mass density contour lines at  $t = 1.5$  and  $t = 2.0$ .



(a) Adapted  $h = 0.05$  mesh at  $t = 1.5$ .



(b) Adapted  $h = 0.05$  mesh at  $t = 2.0$ .

fig:meshsphere2

Figure 20: Shock-sphere interaction adapted meshes at  $t = 1.5$  and  $t = 2.0$ .

587 a projection step on the curved boundary parametric model. The iterative correction  
588 scheme allows to obtain valid meshes both in the volume and on the curved bound-  
589 aries, and does not depend either on the specific choice of the mesh PDE model or the  
590 boundary geometry representation.

591 The reference domain formulation for mesh movement produces sufficiently adapted  
592 meshes in as few as ten Jacobi iterations per time step during an unsteady flow sim-  
593 ulation. While the a-posteriori relaxation algorithm is akin to a forward substitution  
594 algorithm, and thus formally dependent from the node ordering, this doesn't appear  
595 to spoil the adaptation pattern in any of our tests. We show the successful genera-  
596 tion of valid adapted mesh on three-dimensional cases with moving shock waves. While  
597 the computational time overhead with respect to the original unadapted mesh is non-  
598 negligible, it is more than acceptable when compared to the simulation times needed  
599 to achieve the same accuracy on discontinuous flow features on uniformly refined mesh.  
600 The attractiveness of the method rests in fact in its applicability on moving shocks,  
601 where an off-line mesh refinement approach would require to refine the mesh in most of  
602 the computational domain, and its easy coupling with ALE solvers, enabling solution  
603 conservation on the adapted meshes.

604 Limitations of this **r-adaptation** method are the same of the original two-dimensional  
605 formulation, namely the Laplacian models excessively pulls nodes towards non-convex  
606 boundaries and the displacement uncoupling in the multiple space directions can create  
607 sensible adaptation patterns for excessively strong adaptation parameters. **Also, the**  
608 **choice of the parameters of the monitor function appear to be application dependent.**  
609 **possibly leading to excessive mesh stretching for same values of the parameters.** In  
610 these extreme situations, the effect of the **novel** a-posteriori relaxation scheme allows  
611 nonetheless to recover a valid mesh by blocking mesh displacement in critical zones,  
612 allowing to continue the mesh movement at successive time steps as the flow features  
613 evolve away from the blocked mesh elements. **We would like to remark that our limiting**  
614 **procedure is targeted at preserving mesh validity throughout the adaptation procedure.**  
615 **This means that a nodal displacement can be blocked if the volume of an adjacent**  
616 **element falls below an user-defined threshold, but the mesh remains valid. Thus, the**  
617 **vertex positions of the blocked elements can be relaxed either by a subsequent application**  
618 **of r-adaptation at the next time step as the monitor function moves (as it is often the case**  
619 **in the simulation of traveling waves), either by the application of standard smoothing**  
620 **algorithms, which are fundamentally simpler than untangling methods.**

621 While a linear finite element approximation is sufficient to model the nodal degrees  
622 of freedom of straight-sided meshes, generalizations of the a-posteriori limiting method  
623 to curved meshes can be envisaged by increasing the degree of the finite element ba-  
624 sis. This would require the formulation of a volume positivity predicate for the curved  
625 tetrahedron, which is outside the scope of this work.

626 The developments shown in this work have been primarily motivated by their ap-  
627 plication to capturing moving shock waves in inviscid compressible flows. However,  
628 r-adaptation can have interesting applications also to viscous flows, as preliminary  
629 work [36] shows that vorticity-based sensors allow capturing vortical structures in sep-  
630 arated flows. This, together with the critical treatment of boundary layers in turbulent

631 flow computations, will be investigated in the future. Future research lines also include  
632 the parallelization of the current method, for which no specific problems are envisaged,  
633 and the study of r-adaptation as a tool to complement h-adaptation in time-dependent  
634 simulations to somewhat reduce the overhead of the adaptation strategy.

## 635 Acknowledgements

636 We would like to recognize the fundamental contribution our colleague and friend  
637 Cécile Dobrzynski brought to this work.

## 638 References

MmgSW  
640

[1] *Mmg software for simplicial remeshing*, SWHID: swh:1:dir:0ea5ec4a0e978d49debf27878cf2c55629101977;  
REPOSITORY: <https://github.com/MmgTools/mmg>.

AlauzetFrey2003  
642

[2] Frédéric Alauzet and Pascal Frey, *Estimateur d'erreur géométrique et métriques anisotropes pour l'adaptation de maillage. Partie I : aspects théoriques*, Research Report RR-4759, INRIA, 2003.

Alauzet2016  
644

[3] Frédéric Alauzet, *A parallel matrix-free conservative solution interpolation on unstructured tetrahedral meshes*, Computer Methods in Applied Mechanics and Engineering **299** (2016), 116 – 142.

aia:hal-01102124  
646  
647

[4] Luca Arpaia and Mario Ricchiuto, *Mesh adaptation by continuous deformation. basics: accuracy, efficiency, well balancedness*, Research Report RR-8666, Inria Bordeaux Sud-Ouest ; INRIA, January 2015.

aia:hal-01372496  
648  
649

[5] Luca Arpaia and Mario Ricchiuto, *r-adaptation for shallow water flows: conservation, well balancedness, efficiency*, Computers & Fluids **160** (2018), 175 – 203.

Arpaia2020  
651

[6] ———, *Well balanced residual distribution for the ALE spherical shallow water equations on moving adaptive meshes*, Journal of Computational Physics **405** (2020), 109173.

Brackbill1993  
653

[7] J.U. Brackbill, *An adaptive grid with directional control*, Journal of Computational Physics **108** (1993), no. 1, 38 – 50.

Bryson1961  
655

[8] A. E. Bryson and R. W. F. Gross, *Diffraction of strong shocks by cones, cylinders, and spheres*, Journal of Fluid Mechanics **10** (1961), no. 1, 1–16.

Budd2009  
657

[9] Chris J. Budd, Weizhang Huang, and Robert D. Russell, *Adaptivity with moving grids*, Acta Numerica **18** (2009), 111–241.

Ceniceros2001  
659

[10] Hector D. Cenicerros and Thomas Y. Hou, *An efficient dynamically adaptive mesh for potentially singular solutions*, Journal of Computational Physics **172** (2001), no. 2, 609 – 639.

Chen2008  
661  
662

[11] Guoxian Chen, Huazhong Tang, and Pingwen Zhang, *Second-order accurate godunov scheme for multicomponent flows on moving triangular meshes*, Journal of Scientific Computing **34** (2008), no. 1, 64–86.

Dapogny2014  
664  
665

[12] C. Dapogny, C. Dobrzynski, and P. Frey, *Three-dimensional adaptive domain remeshing, implicit domain meshing, and applications to free and moving boundary problems*, Journal of Computational Physics **262** (2014), 358 – 378.

Donea2004  
667

[13] Jean Donea, Antonio Huerta, J.-Ph. Ponthot, and A. Rodríguez-Ferran, *Arbitrary lagrangian-eulerian methods*, John Wiley & Sons, Ltd, 2004.



- Drikakis1997**  
669  
670 [14] D. Drikakis, D. Ofengeim, E. Timofeev, and P. Voionovich, *Computation of non-stationary shock-wave/cylinder interaction using adaptive-grid methods*, Journal of Fluids and Structures **11** (1997), no. 6, 665 – 692.
- Dvinsky1991**  
672 [15] Arkady S Dvinsky, *Adaptive grid generation from harmonic maps on riemannian manifolds*, Journal of Computational Physics **95** (1991), no. 2, 450 – 476.
- Dwight2009**  
674  
675 [16] Richard P. Dwight, *Robust mesh deformation using the linear elasticity equations*, Computational Fluid Dynamics 2006 (Berlin, Heidelberg) (Herman Deconinck and E. Dick, eds.), Springer Berlin Heidelberg, 2009, pp. 401–406.
- Emery1968**  
677 [17] Ashley F Emery, *An evaluation of several differencing methods for inviscid fluid flow problems*, Journal of Computational Physics **2** (1968), no. 3, 306 – 331.
- Farhat2001**  
679  
680 [18] Charbel Farhat, Philippe Geuzaine, and Céline Grandmont, *The discrete geometric conservation law and the nonlinear stability of ale schemes for the solution of flow problems on moving grids*, Journal of Computational Physics **174** (2001), no. 2, 669 – 694.
- FarrellMaddison2011**  
682 [19] P.E. Farrell and J.R. Maddison, *Conservative interpolation between volume meshes by local galerkin projection*, Computer Methods in Applied Mechanics and Engineering **200** (2011), no. 1, 89 – 100.
- Fortunato2016**  
684 [20] Meire Fortunato and Per-Olof Persson, *High-order unstructured curved mesh generation using the winslow equations*, J. Comput. Phys. **307** (2016), no. C, 1–14.
- FreyGeorge2007**  
686 [21] Pascal Jean Frey and Paul-Louis George, *Mesh generation: Application to finite elements*, ISTE, 2007.
- Guardone2011**  
688  
689 [22] A. Guardone, D. Isola, and G. Quaranta, *Arbitrary lagrangian eulerian formulation for two-dimensional flows using dynamic meshes with edge swapping*, Journal of Computational Physics **230** (2011), no. 20, 7706 – 7722.
- GuillardFarhat2000**  
691  
692 [23] Hervé Guillard and Charbel Farhat, *On the significance of the geometric conservation law for flow computations on moving meshes*, Computer Methods in Applied Mechanics and Engineering **190** (2000), no. 11, 1467 – 1482.
- Hansen2004**  
694 [24] Glen Hansen, Andrew Zardecki, Doran Greening, and Randy Bos, *A finite element method for unstructured grid smoothing*, Journal of Computational Physics **194** (2004), no. 2, 611 – 631.
- Hermes2018**  
695 [25] D. Hermes and P.-O. Persson, *High-order solution transfer between curved triangular meshes*, 2018.
- Huang2001**  
697 [26] Weizhang Huang, *Variational mesh adaptation: Isotropy and equidistribution*, Journal of Computational Physics **174** (2001), no. 2, 903 – 924.
- Huang2018**  
699 [27] Weizhang Huang and Lennard Kamenski, *On the mesh nonsingularity of the moving mesh pde method*, no. 87, 1887–1911.
- Huang2011**  
701 [28] Weizhang Huang and Robert D. Russell, *Adaptive moving mesh methods*, Applied Mathematical Sciences **174** (2011), no. 174, Applied Mathematical Sciences.
- Isola2015**  
703 [29] D. Isola, A. Guardone, and G. Quaranta, *Finite-volume solution of two-dimensional compressible flows over dynamic adaptive grids*, Journal of Computational Physics **285** (2015), 1 – 23.
- JohnsonTezduyar1994**  
705  
706 [30] A.A. Johnson and T.E. Tezduyar, *Mesh update strategies in parallel finite element computations of flow problems with moving boundaries and interfaces*, Computer Methods in Applied Mechanics and Engineering **119** (1994), no. 1, 73 – 94.
- Knupp1993**  
708 [31] P. Knupp and S. Steinberg, *Fundamentals of grid generation*, The Fundamentals of Grid Generation, Taylor & Francis, 1993.

- [arikShashkov2008](#) [32] M. Kucharik and M. Shashkov, *Extension of efficient, swept-integration-based conservative remapping method for meshes with changing connectivity*, International Journal for Numerical Methods in Fluids **56** (2008), no. 8, 1359–1365.  
710  
711
- [rik2003efficient](#) [33] Milan Kucharik, Mikhail Shashkov, and Burton Wendroff, *An efficient linearity-and-bound-preserving remapping method*, Journal of Computational Physics **188** (2003), no. 2, 462–471.  
713
- [Li2002](#) [34] Ruo Li, Tao Tang, and Pingwen Zhang, *A moving mesh finite element algorithm for singular problems in two and three space dimensions*, Journal of Computational Physics **177** (2002), no. 2, 365 – 393.  
715  
716
- [Liao1992](#) [35] G. Liao, *Variational approach to grid generation*, Numerical Methods for Partial Differential Equations **8** (1992), no. 2, 143–147.  
718
- [eau:tel-01500093](#) [36] Leo Nouveau, *Adaptive residual based schemes for solving the penalized Navier Stokes equations with moving bodies : application to ice shedding trajectories*, Theses, Université de Bordeaux, December 2016.  
720  
721
- [Park2016](#) [37] Michael A. Park, Adrien Loseille, Joshua Krakos, Todd R. Michal, and Juan J. Alonso, *Unstructured grid adaptation: Status, potential impacts, and recommended investments towards cfd 2030*, AIAA AVIATION Forum, American Institute of Aeronautics and Astronautics, June 2016, pp. –.  
723  
724
- [Re2017](#) [38] B. Re, C. Dobrzynski, and A. Guardone, *An interpolation-free ale scheme for unsteady inviscid flows computations with large boundary displacements over three-dimensional adaptive grids*, Journal of Computational Physics **340** (2017), 26 – 54.  
726  
727
- [Sun2005](#) [39] M Sun, T Saito, K Takayama, and H Tanno, *Unsteady drag on a sphere by shock wave loading*, Shock waves **14** (2005), no. 1-2, 3-9.  
729
- [Tang2003](#) [40] Huazhong Tang and Tao Tang, *Adaptive mesh methods for one- and two-dimensional hyperbolic conservation laws*, SIAM Journal on Numerical Analysis **41** (2003), no. 2, 487–515.  
731
- [Tang2005](#) [41] Tao Tang, *Moving mesh methods for computational fluid dynamics*, Contemporary mathematics **383** (2005), 141–174.  
733
- [Tanno2003](#) [42] H Tanno, K Itoh, T Saito, A Abe, and K Takayama, *Interaction of a shock with a sphere suspended in a vertical shock tube*, Shock Waves **13** (2003), no. 3, 191–200.  
735
- [thomasLombard1979](#) [43] PD Thomas and CK Lombard, *Geometric conservation law and its application to flow computations on moving grids*, AIAA journal **17** (1979), no. 10, 1030–1037.  
737
- [Thompson1985](#) [44] J.F. Thompson, Z.U.A. Warsi, and C.W. Mastin, *Numerical grid generation: foundations and applications*, North-Holland, 1985.  
739
- [TTM1977](#) [45] Joe F Thompson, Frank C Thames, and C Wayne Mastin, *Tomcat — a code for numerical generation of boundary-fitted curvilinear coordinate systems on fields containing any number of arbitrary two-dimensional bodies*, Journal of Computational Physics **24** (1977), no. 3, 274 – 302.  
741  
742
- [pson1977boundary](#) [46] Joe F Thompson, Frank C Thames, and Charles Wayne Mastin, *Boundary-fitted curvilinear coordinate systems for solution of partial differential equations on fields containing any number of arbitrary two-dimensional bodies*, Tech. Report NASA-CR-2729, NASA, 1977.  
744  
745
- [Toulorge2013](#) [47] Thomas Toulorge, Christophe Geuzaine, Jean-François Remacle, and Jonathan Lambrechts, *Robust untangling of curvilinear meshes*, Journal of Computational Physics **254** (2013), 8 – 26.  
747
- [Trulio1961](#) [48] John G Trulio and Kenneth R Trigger, *Numerical solution of the one-dimensional lagrangian hydrodynamic equations*, Tech. report, California. Univ., Livermore, CA (United States). Lawrence Radiation Lab., 1961.  
749  
750

- Turner2018**<sub>752</sub>  
753 [49] Michael Turner, Joaquim Peiró, and David Moxey, *Curvilinear mesh generation using a variational framework*, Computer-Aided Design **103** (2018), 73 – 91, 25th International Meshing Roundtable Special Issue: Advances in Mesh Generation.
- Leer1979**<sub>755</sub> [50] Bram van Leer, *Towards the ultimate conservative difference scheme. v. a second-order sequel to godunov's method*, Journal of Computational Physics **32** (1979), no. 1, 101 – 136.
- Vlachos2001**<sub>757</sub>  
758 [51] Alex Vlachos, Jörg Peters, Chas Boyd, and Jason L. Mitchell, *Curved pn triangles*, Proceedings of the 2001 Symposium on Interactive 3D Graphics (New York, NY, USA), I3D '01, Association for Computing Machinery, 2001, p. 159–166.
- Winslow1981**<sub>760</sub> [52] Alan M Winslow, *Adaptive-mesh zoning by the equipotential method*, Tech. report, Lawrence Livermore National Lab., CA (USA), 1981.
- WoodwardColella1984**<sub>762</sub> [53] P. Woodward and P. Colella, *The numerical simulation of two-dimensional fluid flow with strong shocks*, Journal of Computational Physics **54** (1984), 115–173.
- Etienne2009**<sub>764</sub>  
765 [54] S. Étienne, A. Garon, and D. Pelletier, *Perspective on the geometric conservation law and finite element methods for ale simulations of incompressible flow*, Journal of Computational Physics **228** (2009), no. 7, 2313 – 2333.